Atmospheric
Chemistry
and Physics

Upper-tropospheric pollutants observed by MIPAS: geographic and seasonal variations

Norbert Glatthor[1], Gabriele P. Stiller[1], Thomas von Clarmann[1,✝], Bernd Funke[2], Sylvia Kellmann[1], and Andrea Linden[1,✝]

[1]Karlsruhe Institute of Technology, Institute of Meteorology and Climate Research, Karlsruhe, Germany
[2]Instituto de Astrofísica de Andalucía, CSIC, Granada, Spain
✝deceased, Thomas von Clarmann on 13 January 2024 and Andrea Linden on 18 November 2024

Correspondence: Norbert Glatthor (norbert.glatthor@kit.edu)

Abstract. We present a global climatology of upper-tropospheric hydrogen cyanide (HCN), carbon monoxide (CO), acetylene (C_2H_2), ethane (C_2H_6), peroxyacetyl nitrate (PAN), and formic acid (HCOOH) obtained from observations of the Michelson Interferometer for Passive Atmospheric Sounding (MIPAS) on board the Environmental Satellite (Envisat) between 2002 and 2012. At northern midlatitudes and high latitudes, the biomass burning tracer HCN, but also CO, PAN, and HCOOH, exhibit maxima during spring and/or summer and minima during winter. On the contrary, maximum northern extratropical C_2H_2 and C_2H_6 amounts were measured during winter and spring, and minimum values were measured during summer and fall. In the tropics and subtropics, enhanced amounts of all pollutants were observed during all seasons, especially widespread and up to southern midlatitudes during austral spring. Other characteristic features are eastward transport of anthropogenic C_2H_6 and of biogenic HCOOH from Central and North America in boreal summer, accumulation of pollutants in the Asian monsoon anticyclone (AMA), and enhanced C_2H_2 over southeastern Asia in boreal winter. Clear indication of biogenic release of HCOOH was also found above tropical South America and Africa. A global correlation analysis of the other pollutants with HCN corroborates common release by biomass burning as a source of the widespread southern hemispheric pollution during austral spring. Furthermore, high correlation with HCN points to biomass burning as a major source of tropical and subtropical C_2H_2 and PAN during most of the year. In the northern extratropics, there are generally low correlations with HCN during spring and early summer, indicating the influence of anthropogenic and biogenic sources. However, in August, there are stronger correlations above Siberia and boreal North America, which points to common release by boreal fires. This is confirmed by the respective enhancement ratios (ERs). The ERs measured above northeastern Africa fit well to the emission ratios of the dominant local fire type (savanna burning) for C_2H_2, while those for CO, C_2H_6, and HCOOH rather indicate tropical forest fires or additional anthropogenic or biogenic sources. The southern hemispheric $\Delta C_2H_6/\Delta HCN$ ERs obtained during August to October are in good agreement with the emission ratio for savanna fires. The same applies for $\Delta C_2H_2/\Delta HCN$ in August and for $\Delta HCN/\Delta CO$ and $\Delta HCOOH/\Delta HCN$ in October.

1   Introduction

Hydrogen cyanide (HCN) is regarded as an almost unambiguous tracer of biomass burning (Li et al., 2003; Singh et al., 2003; Yokelson et al., 2007; Lupu et al., 2009), while the other trace gases presented here generally have additional sources, too. HCN has a tropospheric lifetime of 5–6 months, which is controlled by ocean uptake (Li et al., 2000, 2003; Singh et al., 2003). Carbon monoxide (CO) is released from traffic, industry, and biomass burning by incomplete combustion processes and is a precursor of tropospheric ozone. However, approximately one-half of its tropospheric burden originates from in situ photochemical production by oxidation of methane and more complex hydrocarbons (Park et al., 2013). Because of its relatively long lifetime of about 2 months, CO has often been used as a tracer for the transport of tropospheric pollution (Rinsland et al., 1998; Edwards et al., 2006; Funke el al., 2009). Its upper-tropospheric concentrations are generally much higher than those of the other trace gases presented here. Acetylene (C_2H_2) is a relatively reliable but not unique tracer of biomass burning (Blake et al., 1996; Singh et al., 1996). More recent studies (Streets et al., 2003; Xiao et al., 2007) indicate biofuel emissions from cooking fires or residential heating as its dominant source. Xiao et al. (2007) assume a global biofuel source of 50 % and global fossil fuel and biomass burning sources of 25 % each. The upper-tropospheric lifetime of C_2H_2 is about 2 weeks at low latitudes or during extratropical summer (Xiao et al., 2007). During winter, its lifetime increases considerably at higher latitudes due to the absence of the hydroxyl radical (OH) under less sunlit conditions. Ethane (C_2H_6) is the most abundant tropospheric non-methane hydrocarbon (Singh et al., 2001). Rudolph (1995) indicates biomass burning and natural gas losses as its major sources, with releases of 6.4 and $6 \, \mathrm{Tg \, yr^{-1}}$, respectively. According to Xiao et al. (2008), the major source of C_2H_6 is fossil fuel production (62 %), followed in about equal parts by biofuel and biomass burning. Its mean atmospheric lifetime is approximately 2 months (Hough, 1991) but 6 to 10 months in the extratropical upper troposphere (UT) during winter (Xiao et al., 2008; Helmig et al., 2016). Peroxyacetyl nitrate (PAN; $CH_3C(O)OONO_2$) is formed via the oxidation of hydrocarbons and subsequent reaction with NO_2 and is thus generated in air masses polluted by fuel emissions or by biomass burning (Singh et al., 1996; Gaffney et al., 1999). Fischer et al. (2014) emphasize the importance of lightning NO_x for the production of PAN. Furthermore, according to these authors, the most important precursor of PAN is isoprene (37 %), which is mainly released from plant foliage (Guenther et al., 2006). Other precursors are acetone (9 %) and ethane (6 %). The lifetime of PAN is highly temperature-dependent and can be up to several months in the cold upper troposphere (Singh, 1987). It is the major reservoir of tropospheric NO_x (NO and NO_2) and enables the transport of NO_x to remote tropospheric areas. Direct sources of formic acid (HCOOH) are biogenic

release, anthropogenic emissions (biofuel or fossil fuel burning), and biomass burning (Grutter et al., 2010, and references therein). While Grutter et al. (2010) state that the relative contribution of direct emissions and chemical transformations is unknown, the oxidation of hydrocarbons is declared as the dominant source of atmospheric HCOOH in other publications (Sanhueza et al., 1996, and references therein). According to Stavrakou et al. (2012), the contribution of biogenic sources (tropical and boreal forests) to atmospheric HCOOH is as high as 90 %. Franco et al. (2020) state strong biogenic sources in tropical spring and northern extratropical spring and summer.

In the following, we regard the observation of enhanced HCN amounts as an almost unique indication of pollution by biomass burning. A high correlation of any other trace gas with enhanced HCN points to biomass burning as an important source of this pollutant, as well. The measurement of high C_2H_2 volume mixing ratios (VMRs) in combination with low HCN amounts hints at biofuel or fossil fuel burning. The exclusive measurement of high C_2H_6 amounts hints at release during the production or transport of oil and gas. The measurement of enhanced PAN or HCOOH not correlated with elevated HCN points to biogenic sources or anthropogenic emissions other than biomass burning of these trace gases.

Two other spaceborne datasets containing most of the pollutants presented here result from measurements of the Atmospheric Chemistry Experiment/Fourier Transform Spectrometer (ACE-FTS) on SCISAT (Bernath et al., 2005; Boone et al., 2005) and of the Infrared Atmospheric Sounding Interferometer (IASI) on MetOp-A (Blumstein et al., 2004; Hilton et al., 2012). ACE-FTS is a limb sounder performing solar occultation measurements in the spectral range of 750–4400 $\mathrm{cm^{-1}}$. ACE-FTS measurements of HCN were presented by Lupu et al. (2009). Glatthor et al. (2015) performed a comparison between HCN observed by the Michelson Interferometer for Passive Atmospheric Sounding (MIPAS) and by ACE-FTS. González Abad et al. (2009) discuss seasonal latitude–height cross-sections of HCOOH; González Abad et al. (2011) discuss those of CO, C_2H_6, and C_2H_2; and Tereszchuk et al. (2013b) discuss those of PAN observed by ACE-FTS. A climatological analysis of the trace gases CO, C_2H_6, C_2H_2, and HCN in the upper troposphere and lower stratosphere was performed by Park et al. (2013) but focused on the tropics only. IASI is a nadir sounder covering the infrared spectral region from 645 to 2760 $\mathrm{cm^{-1}}$, which carries out cross-track scans with a swath width of $\sim 2400 \, \mathrm{km}$. Observations of tropospheric trace gases by IASI are generally presented as column amounts. Spatial distributions of CO observed by IASI were presented by Clerbaux et al. (2009), those of tropical and subtropical HCN and C_2H_2 of IASI were shown by Duflot et al. (2015), and those of HCOOH were presented by Pommier et al. (2016) and Franco et al. (2020).

In the following, we will briefly describe MIPAS, the retrieval setups, and the method of tropopause calculation. Then, we will present seasonal global distributions of the pollutants on a surface at 3 km below the tropopause. Furthermore, we will discuss the monthly variation in zonally averaged time series. By means of global correlation analyses with HCN, we will discriminate between biomass burning and other anthropogenic or biogenic sources of the individual pollutants. The enhancement ratios (ERs) resulting from the correlation analyses will be compared with enhancement ratios obtained from ACE-FTS measurements and with emission ratios derived from published emission factors. Our presentation will be restricted to seasonal and monthly composites of the whole MIPAS dataset. Interannual variations in, for example, MIPAS HCN were described by Glatthor et al. (2015). Additionally, some monthly distributions of correlation coefficients and ERs obtained for individual years will be presented in the Supplement. The paper will finish with a summary and conclusions.

2 MIPAS measurements

2.1 Instrument description

The Michelson Interferometer for Passive Atmospheric Sounding (MIPAS) was operated on board the European polar-orbiting Environmental Satellite (Envisat) from July 2002 until April 2012. MIPAS was a Fourier-transform infrared (FTIR) emission spectrometer with a measurement range from 685 to 2410 cm^{-1}, which enabled the observation of numerous trace gases emitting in the mid-infrared spectral region (European Space Agency, ESA, 2000; Fischer et al., 2008). Due to its measuring principle, MIPAS was able to observe the atmosphere in global coverage during day and night.

Until March 2004, MIPAS was operated with a spectral resolution of 0.025 cm^{-1} (unapodized) in the so-called full-resolution (FR) mode. After a data gap due to technical problems during the rest of the year 2004, MIPAS was run with a spectral resolution of 0.0625 cm^{-1} in reduced-resolution (RR) mode from January 2005. We present data of the FR and RR nominal modes and of the RR upper troposphere and lower stratosphere 1 (UTLS-1) mode with horizontal sampling distances of 510, 410, and 290 km, respectively. The nominal modes consisted of rearward limb scans covering the altitude ranges 6–68 km (FR) and 7–72 km (RR). The UTLS-1 mode was restricted to the altitude region 5.5–49 km. The tangent height distance of the FR mode was 3 km up to 42 km and increased up to 8 km between the two uppermost tangents. The step width of the RR nominal mode was 1.5 km up to 22 km and then increased to 2, 3, and 4–5 km in the upper part of the scan. The step width of the RR UTLS-1 mode was 1.5 km up to 19 km, 2 km up to 25 km, and increasingly wider above.

2.2 Retrieval method and error estimation

Retrievals were performed with the processor of the Institute of Meteorology and Climate Research (IMK) and the Instituto de Astrofísica de Andalucía (IAA) by use of level-1B radiance spectra of data version 5.02/5.06 (reprocessed data) provided by the European Space Agency (ESA) (Nett et al., 2002). The central components of the retrieval processor are the Karlsruhe Optimized and Precise Radiative transfer Algorithm (KOPRA) (Stiller, 2000) for radiative transfer calculations and the Retrieval Control Program (RCP) of IMK/IAA for inverse modeling. The inversion consists of the determination of vertical profiles of atmospheric state parameters by constrained non-linear least-squares fitting in a global-fit approach (von Clarmann et al., 2003). The general approach of MIPAS data processing at IMK has been described in various papers, e.g., von Clarmann et al. (2003), Höpfner et al. (2004) or von Clarmann et al. (2009).

The retrieval of the trace species presented here is described in previous papers (Glatthor et al., 2007, 2009, 2015; von Clarmann et al., 2009; Funke el al., 2009; Grutter et al., 2010; Wiegele et al., 2012). The data versions used in this presentation are compiled in Table 1. Since the altitude spacing of the retrieval grid chosen is finer than the height distance between the tangent altitudes, potential instabilities have to be attenuated by the application of a constraint. For this purpose, Tikhonov's first derivative operator was used (Tikhonov, 1963; Steck, 2002). Instead of climatological a priori profiles, height-constant profiles were chosen to avoid any influence of the a priori information on the shape of the retrieved profiles. Generally, profiles of the main interfering trace gases were jointly fitted along with the target species. Additional retrieval variables were microwindow-dependent continuum radiation profiles and microwindow-dependent, but height-independent, zero-level calibration corrections. If available, the radiative contribution of other interfering gases was modeled by using their profiles retrieved in preceding steps in the processing sequence. When no pre-fitted profiles were available, we used the climatology compiled by Remedios et al. (2007) for this purpose. MIPAS measurements provide information on the trace gases presented here from the free troposphere up to about 25 km for C_2H_2, C_2H_6, and PAN; up to about 45 km for HCN; and up to 70 km (nominal-mode scans) for CO. The vertical resolution of the different pollutants in the altitude region displayed in the following sections (2–3 km below the tropopause, which, dependent on latitude, corresponds to geometrical altitudes of $\sim$ 8–14 km) is displayed in Table 2. At 8 km in the northern extratropics, it varies between 2.3 km (PAN) and 4.3 km (HCN), and, at 14 km in the southern hemispheric tropics and subtropics, it varies between 2.8 km (PAN) and 4–4.5 km (HCN, CO, C_2H_6). Table 2 also contains the estimated standard deviation (ESD), which is the measurement noise transformed into parameter space by the retrieval program. The ESD is later used to determine the λ values in the regression analyses.

The total retrieval errors for significantly enhanced VMRs of these pollutants in the upper troposphere are between 5 % and 15 %. More details on error estimation and vertical resolution are given in the publications mentioned above.

3 Tropopause height derived from MIPAS temperature profiles

To enable a tropopause-related presentation of the pollutants, we calculated the thermal tropopause for each MIPAS scan from the temperature profile retrieved in an earlier step of the processing chain. The calculation of the thermal tropopause was performed according to the definition of the World Meteorological Organization (WMO). In this definition, the tropopause is the lowest level, at which the lapse rate $-\mathrm{d}T/\mathrm{d}z$ decreases to $2\,\mathrm{K\,km^{-1}}$ or less and does not exceed this value in an overlying layer of the width of at least 2 km. Technically, we determined the tropopause as described in Zängl and Hoinka (2001, their Eq. A1). This means that lapse rate profiles were calculated as centered difference quotients between each two adjacent retrieval heights. Then, the lowest lapse rate level with $-\mathrm{d}T/\mathrm{d}z \leq 2\,\mathrm{K\,km^{-1}}$ was searched. The tropopause height was determined by linear interpolation between the lapse rate at this level and the level below to the $2\,\mathrm{K\,km^{-1}}$ value, provided the criterion for layer width was fulfilled. If the latter criterion was not met, the next level with $-\mathrm{d}T/\mathrm{d}z \leq 2\,\mathrm{K\,km^{-1}}$ was checked. In a subsequent step, the retrieved profiles of the pollutants were related to the individual tropopause heights.

Figure 1 shows geographical distributions of seasonal tropopause heights averaged over the whole MIPAS dataset. The tropical tropopause height is about 16.5 km during summer and fall and around 17 km in winter and spring. Around 30–40° N and 30–40° S, the tropopause height decreases strongly, reaching a level of 8–9 km at high northern latitudes and 8–12.5 km at high southern latitudes. Compared to the equinoxes, the region of the strongest latitudinal gradient is shifted northward during boreal summer and southward during austral summer. Beside the distinct latitude dependence, the tropopause heights obtained from MIPAS data exhibit a longitudinal variation as well. The most obvious feature is a variation during boreal winter with low tropopause heights above eastern Canada and eastern Siberia and a high tropopause above the North Atlantic and northern Europe, which is connected with oscillations of the polar jet.

At latitudes south of 60° S, the average tropopause height is considerably higher during austral winter (JJA) and spring (SON) than in the remaining part of the year or in the Arctic during boreal winter and spring. This is caused by temperature profiles for which the WMO criterion was not met in the lower atmosphere due to unusually high lapse rates, leading to the determination of tropopause altitudes of up to 20 km. For illustration, we show the individual tropopause heights obtained for the different seasons of the year 2010 in the Sup-

plement (Fig. S1). The disappearance of the Antarctic thermal tropopause during austral winter (July/August) was first reported by Court (1942). Similar problems were reported by, for example, Reichler et al. (2003). To avoid the incorporation of stratospheric data into the upper-tropospheric distributions discussed in the following, we excluded measurements at latitudes south of 50° S for which, during June to August, a tropopause height of more than 13.5 km was determined. Since quite a number of implausibly high tropopause heights were also obtained for Antarctic spring and Arctic winter (see Fig. S1), the same height criterion was applied to measurements at latitudes south of 50° S during September to November and north of 50° N during December to February.

4 Results and discussion

### 4.1 Global distributions at 3 km below the tropopause

In the following, we present global distributions of seasonal composites of the different pollutants at 3 km below the tropopause. This distance was chosen to be sure that, related to the vertical resolution of MIPAS measurements, the distributions are nearly completely tropospheric. The data shown are bin averages ($5° \times 15°$ latitude by longitude, $7.5° \times 15°$ latitude by longitude at the poles) of the whole measurement period of MIPAS (2002–2012). The individual bins typically contain 100 to more than 600 data points at low and midlatitudes but generally much lower numbers (dozens to less then 10) at high latitudes. During strong convection, the tropical bins over the continents contain considerably lower numbers of data points, too.

4.1.1 Hydrogen cyanide (HCN)

During March to May, the climatological HCN distribution exhibits widespread enhancements with mixing ratios of up to 350 parts per trillion by volume (pptv) at northern midlatitudes and partly high latitudes (Fig. 2a). Extensive biomass burning at northern midlatitudes during boreal spring is indicated by fire carbon emissions of the preliminary version 5 of the Global Fire Emissions Database (GFED5) based on burned area from Chen et al. (2023) and fuel consumption from van Wees et al. (2022), added up over the measurement period of MIPAS (Fig. 3a). Strong carbon emissions extend over a large area from eastern Europe over southern to eastern Siberia. According to van der Werf et al. (2010, their Fig. 13), the dominant fire types in this region are agricultural fires in eastern Europe and forest fires in southeastern Siberia. A second region with enhanced carbon emissions in boreal spring extends from the central United States to southern Canada. Other northern hemispheric source regions are southern and southeastern Asia, Central America, and tropical northern Africa. Using trajectory calculations of the Hybrid Single-Particle Lagrangian Integrated Trajectory (HYSPLIT) model of the National Oceanic and At-

Table 1. MIPAS data versions used in the presented analysis. FR: full-resolution measurement mode; RR: reduced-resolution measurement mode; V5H and V5R: spectra version.

Trace gas	FR, nominal mode	RR, nominal mode	RR, UTLS-1 mode
HCN	HCN_V5H_21	HCN_V5R_222/223	HCN_V5R_120
CO	CO_V5H_20	CO_V5H_220/221	CO_V5R_120
C_2H_2	C2H2_V5H_20	C2H2_V5R_221/222	C2H2_V5R_120
C_2H_6	C2H6_V5H_20	C2H6_V5R_220/221	C2H6_V5R_120
PAN	PAN_V5H_21	PAN_V5R_222/223	PAN_V5R_121
HCOOH	HCOOH_V5H_20	HCOOH_V5R_220/221	HCOOH_V5R_120
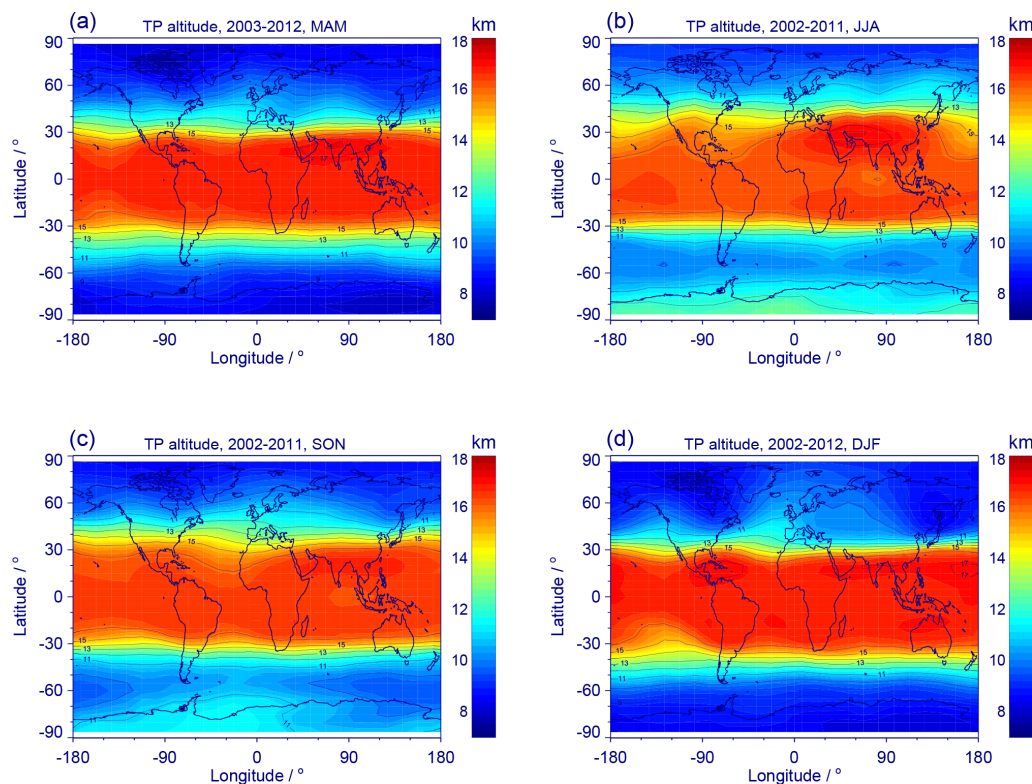
Figure 1. Global distribution of the thermal tropopause derived from MIPAS temperature profiles for the periods **(a)** March to May, **(b)** June to August, **(c)** September to November, and **(d)** December to February. The data are bin averages ($5° \times 15°$ latitude by longitude, $7.5° \times 15°$ latitude by longitude at the poles) of the time period 2002 to 2012.

mospheric Administration (NOAA) (Stein et al., 2015) and fire counts of the Moderate Resolution Imaging Spectroradiometer (MODIS) (Justice et al., 2002) on the Aqua and Terra satellites, individual MIPAS HCN plumes observed at northern midlatitudes during boreal spring could clearly be traced back to sources in northeastern Africa, southeastern Asia, and Central America (Figs. S2–S4 in the Supplement). Although such clear examples for release of discrete HCN plumes from, for example, eastern Europe or southern Siberia could not be found in the samples analyzed so far, a significant contribution of these regions to pollution of the northern extratropical UT by HCN during boreal spring can not be excluded.

The highest northern hemispheric HCN amounts, now also covering the whole Arctic, were measured during June to August (Fig. 2c), with maxima of up to 430 pptv above Siberia and the Canadian Arctic. During this season, the strongest northern hemispheric GFED carbon emissions are located in Siberia and in Canada/Alaska (Fig. 3b), which can be associated to boreal forest fires (van der Werf et al., 2010, their Fig. 13). Other potential source regions are eastern Europe, the Mediterranean area, and the northwestern United States, but contributions from the northern tropics and subtropics strongly decreased. As examples for the transport of HCN from a fire region in western Russia into the polar upper troposphere and for the distribution of enhanced HCN from an-
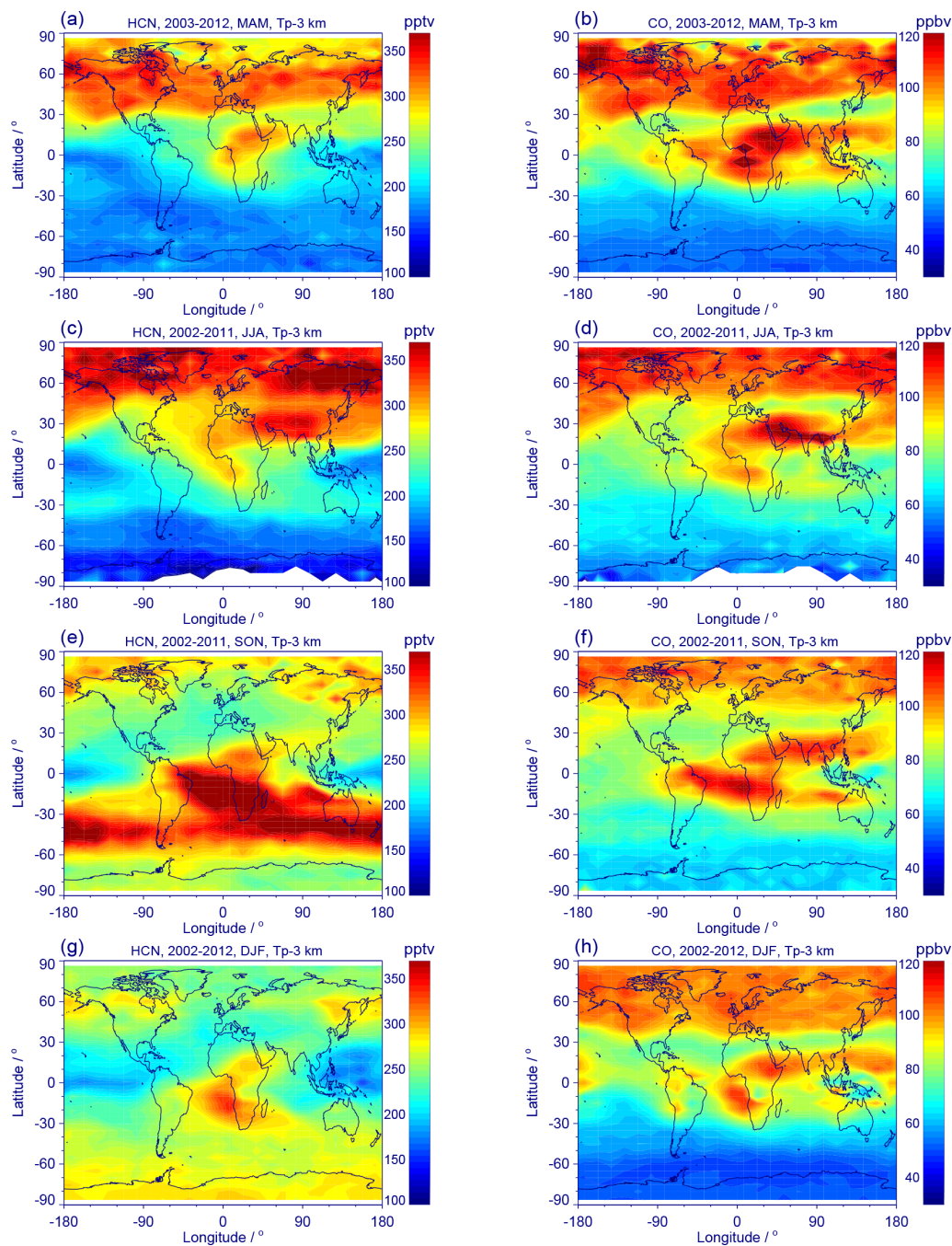
Figure 2. Global HCN distribution measured by MIPAS at 3 km below the tropopause during **(a)** March to May, **(c)** June to August, **(e)** September to November, and **(g)** December to February, as well as the global CO distribution measured by MIPAS at 3 km below the tropopause during **(b)** March to May, **(d)** June to August, **(f)** September to November, and **(h)** December to February. The distributions are averaged over the time period 2002 to 2012.

other region in northeastern Siberia over the Northern Hemisphere (NH), we present MIPAS HCN measurements from August 2008 and 2010 along with respective HYSPLIT trajectories and MODIS fire counts in the Supplement (Figs. S5 and S6).

After the end of the fire season, the HCN amounts in the Northern Hemisphere continuously decline during boreal fall and winter, with especially low amounts over the northern Atlantic and Europe. According to the current state of knowledge (Li et al., 2000, 2003; Singh et al., 2003), low HCN amounts over oceanic regions show the removal of HCN by
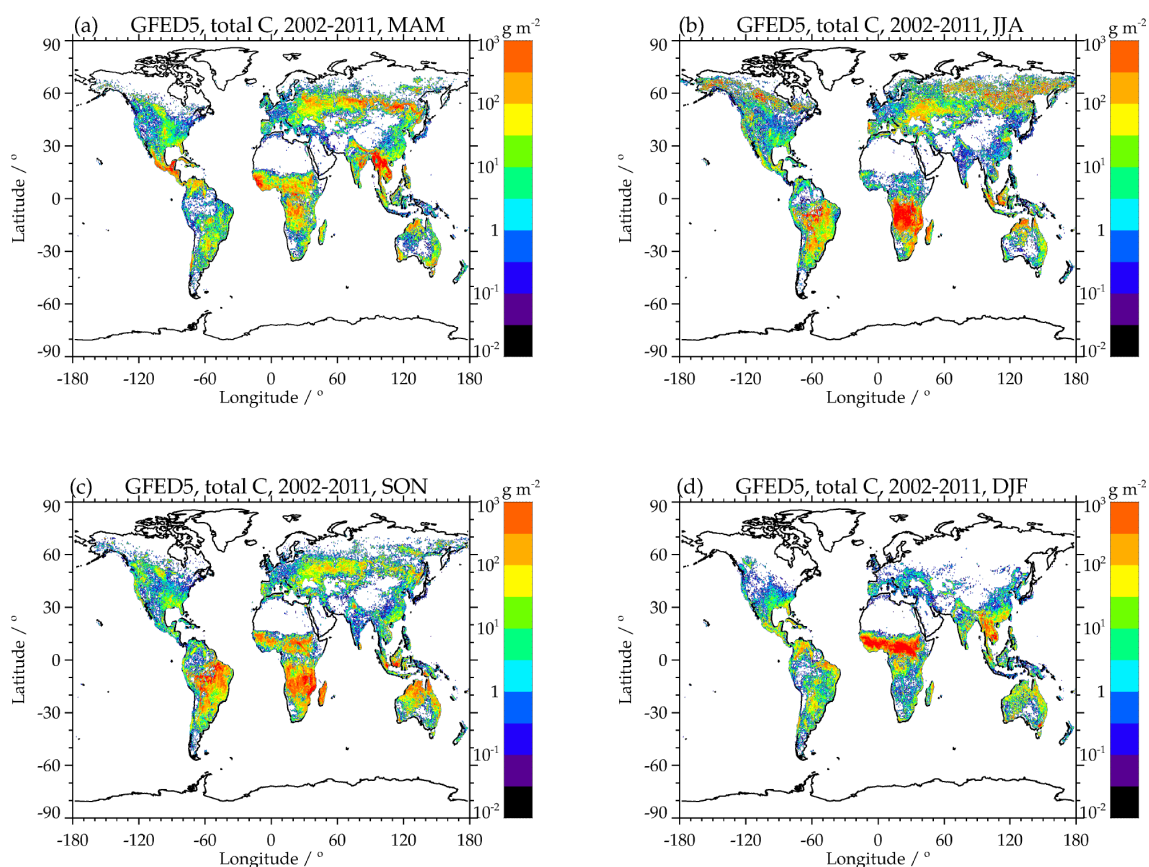
Figure 3. Global carbon emissions by fires of the Global Fire Emissions Database, version 5 (GFEDv5), in $g\,m^{-2}$ during **(a)** March to May, **(b)** June to August, **(c)** September to November, and **(d)** December to February, added up over the measurement period of MIPAS (July 2002–March 2012). The original data are monthly GFEDv5 carbon emissions at 0.25° by 0.25° latitude by longitude spatial resolution.

Table 2. Vertical resolution (VR) in terms of full width at half maximum of the rows of the averaging kernels and estimated standard deviation (ESD) of the different pollutants at the altitudes of 8 km in the northern extratropics and 14 km in the southern tropics.

Trace gas	VR at 8 km / km	VR at 14 km / km	ESD at 8 km / pptv	ESD at 14 km / pptv
HCN	4.5	4.5	28	22
CO	4.2	4.3	1.0×10^4	2.2×10^4
C_2H_2	2.6	3.2	18	12
C_2H_6	3.3	4.3	127	97
PAN	2.3	2.8	23	17
HCOOH	3.0	3.5	23	20

ocean uptake. During boreal winter, the HCN VMRs above the Arctic Ocean also decrease to background levels, while moderately enhanced HCN amounts are located above northeastern China, the North Pacific Ocean, and northern Canada. These enhancements can be remains of the preceding boreal fire season but can also be caused by residential coal burning in eastern Asia as suggested by Singh et al. (2003) and Li et al. (2003).

In the tropics, enhanced HCN amounts were observed above or around Africa during all seasons, which is in line with year-round strong fire activity on this continent. The plume above central and northeastern Africa during March to May, extending eastward towards India, is caused by biomass burning in the savanna region south of the Sahara, which is confirmed by GFED carbon emissions (Fig. 3a). Actually, this process already peaks in boreal winter (see Fig. 3d), but pollutants in this area are more effectively uplifted by increased convection during boreal spring (Duncan et al., 2007; Glatthor et al., 2015). During all seasons, the lowest tropical HCN values (175–200 pptv) were measured above the Pacific due to ocean uptake.

In boreal summer, an HCN plume with VMRs of up to 350 pptv extends from the Arabian Peninsula to eastern China. This feature is caused by the vertical transport of pollution mostly from southern and southeastern Asia within the Asian monsoon region towards the upper troposphere and subsequent confinement inside the Asian monsoon anticyclone (AMA) (see, e.g., Vogel et al., 2015). The slightly lower enhancements over northern Africa and the northern

Pacific reflect the climatological average of eastward and westward outflow.

During September to November, biomass burning shifted towards the Southern Hemisphere (SH), characterized by strongly enhanced HCN amounts in a large region extending from tropical Brazil over southern Africa to the region south of Australia and to the South Pacific. The latitude band between 30 and $60°\,S$ is nearly completely covered with enhanced HCN. Correspondingly, the GFED data show strong fire activities in southern tropical and subtropical South America and Africa (Fig. 3c). There is also an indication of another southern hemispheric plume above the eastern tropical Indian Ocean at $15°\,S$. This feature is caused by strong biomass burning in Indonesia during the years 2002, 2006, and 2009 (see, e.g., Glatthor et al., 2015) with a positive phase of the so-called El Niño–Southern Oscillation (ENSO) (https://www.cpc.ncep.noaa.gov/products/precip/CWlink/MJO/enso.shtml, last access: 20 January 2025) but attenuated by averaging over all years of MIPAS operation. Strong biomass burning in Indonesia and northern Australia during this season is confirmed by the GFED carbon emissions (Fig. 3c). In Fig. S8 in the Supplement, we present HYSPLIT forward trajectories started above the biomass burning regions in South America, southern Africa, and Indonesia, which corroborate the distribution of polluted air masses in the Southern Hemisphere as observed in the MIPAS data.

During December to February, the pollution in the southern tropics and subtropics considerably decreased, and enhanced HCN amounts were mostly restricted to the southern Atlantic and southern Africa. However, due to the time-lagged southward transport of the polluted air masses, maximum HCN amounts of about 270 pptv were measured at high southern latitudes. Similar observations were made by Zeng et al. (2012). In the following two seasons (March to August), the HCN amounts at southern middle and high latitudes continuously decrease to 150 pptv, which we also attribute to ocean uptake.

4.1.2 Carbon monoxide (CO)

The emissions of CO are significantly higher than those of the other pollutants and are therefore presented in parts per billion by volume (ppbv). At northern middle and high latitudes, the highest upper-tropospheric CO amounts of up to 120 ppbv were observed during boreal spring and summer (Fig. 2b and d). This similarity to the HCN cycle points to biomass burning as an important source of enhanced CO. However, the CO amounts in the NH are elevated during the whole year, resulting in a weaker annual variation. This indicates additional anthropogenic sources as well.

Enhanced CO amounts were also found in the tropics and subtropics all the year round in the same regions like elevated HCN, indicating common release by biomass burning. The most prominent signatures in these regions are a plume covering large parts of Africa and extending to southern Asia and the northern subtropical Pacific during March to May, a plume inside the Asian monsoon anticyclone during June to August, and the southern hemispheric biomass burning plume during September to November. Differently to HCN, enhanced CO covers southern and southeastern Asia and the eastern Pacific during the whole year. This hints at a significant fraction of CO from other anthropogenic sources, e.g., in southern and eastern Asia, as well.

Much lower CO VMRs were observed in the southern extratropics. Caused by the southward transport of air masses polluted by biomass burning at southern low latitudes, the CO amounts at southern middle and high latitudes exhibit an annual cycle with moderately enhanced values in austral spring but low values in austral summer and fall. Thus, differently to the longer-lived HCN, the CO amounts at high southern latitudes do not further increase in austral summer but decline instead. Again, this is consistent with the observations of Zeng et al. (2012).

4.1.3 Acetylene (C_2H_2)

The C_2H_2 amounts at northern middle and high latitudes are considerably higher than those observed in the tropics and at southern latitudes (Fig. 4, left column). Differently to HCN, the northern hemispheric C_2H_2 cycle has a maximum of up to 250 pptv during winter and spring and a minimum of 40–80 pptv during summer. This indicates that biomass burning is not the reason for these variations. According to various publications (e.g., Zander et al., 1991; Goldstein et al., 1995; Xiao et al., 2007), the accumulation of C_2H_2 in winter and spring is due to the wintertime minimum of the hydroxyl radical OH, which is the major reactant for the depletion of tropospheric C_2H_2 (Rudolph et al., 1984). An additional cause is the increased domestic heating of biofuel in winter (Streets et al., 2003). During all seasons, but especially during winter and spring, the northern extratropical C_2H_2 amounts show a longitudinal variation, characterized by lower values above the North Atlantic and western Europe and higher values above the Canadian Arctic and eastern Siberia. This feature is correlated with the longitudinal oscillations in tropopause height visible in Fig. 1 and of the polar jet, leading to the northeastward transport of air masses with low C_2H_2 amounts above the northern Atlantic.

The tropical and subtropical C_2H_2 distribution with maximum amounts of up to 120 pptv over Africa and up to 140 pptv in the AMA is spatially well correlated with HCN during all seasons. This points to biomass burning as the dominant source of the enhanced C_2H_2 amounts observed at these latitudes. One exception is southern and southeastern Asia during winter, where, at lower altitudes around 10 km, elevated VMRs of C_2H_2 were observed in combination with low HCN amounts (Fig. A1). This hints to increased biofuel burning during this season. Similarly to HCN, the most widespread southern tropical C_2H_2 pollution, extending from
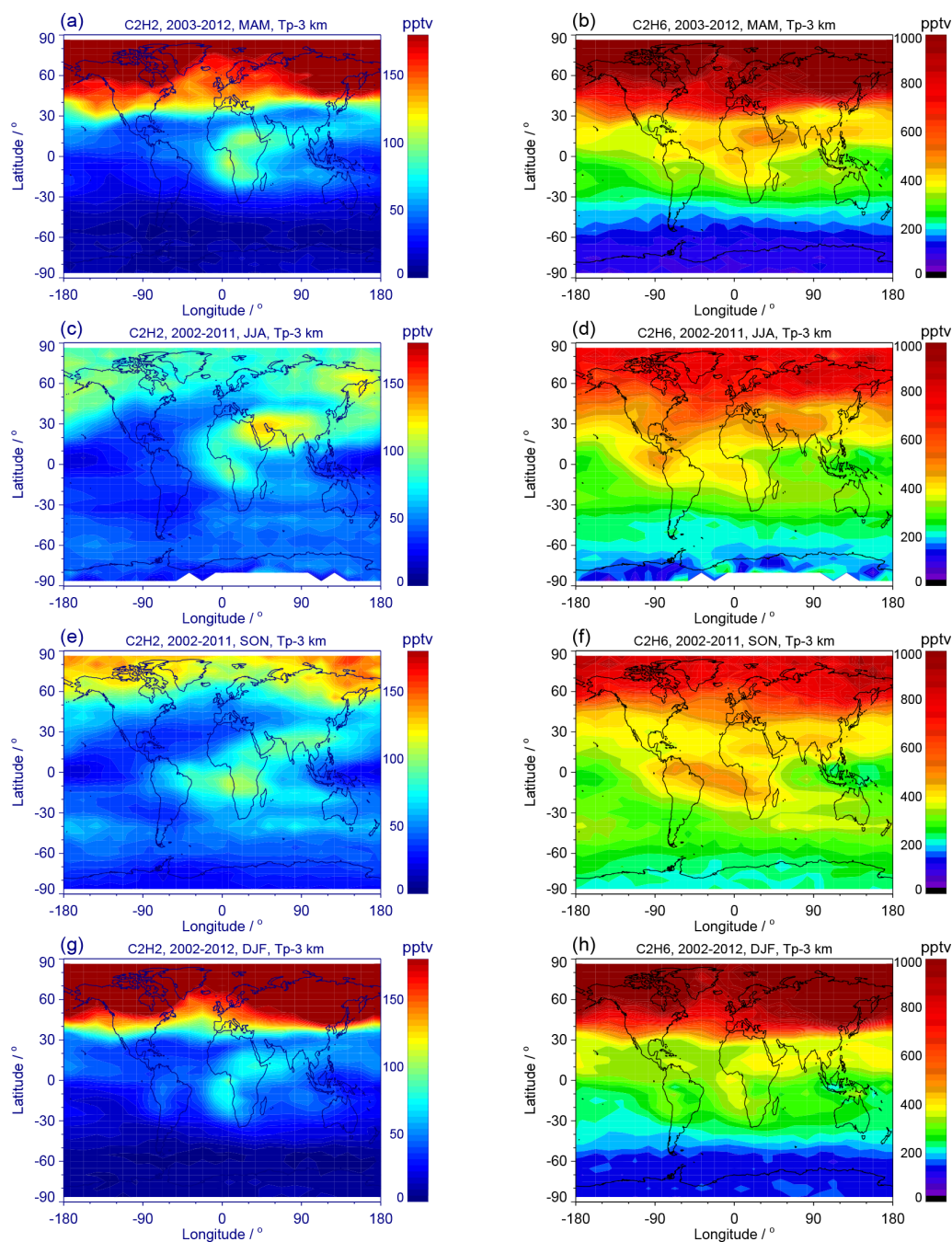
Figure 4. Global C_2H_2 distribution measured by MIPAS at 3 km below the tropopause during **(a)** March to May, **(c)** June to August, **(e)** September to November, and **(g)** December to February, as well as global C_2H_6 distribution measured by MIPAS at 3 km below the tropopause during **(b)** March to May, **(d)** June to August, **(f)** September to November, and **(h)** December to February. The distributions are averaged over the time period 2002 to 2012.

northeastern Brazil over southern Africa to Australia, occurs during September to November.

The C_2H_2 mixing ratios at southern midlatitudes and high latitudes vary between less than 20 pptv during austral summer and fall (December–May) and 40–50 pptv during austral winter (JJA). Shifted by 0.5 years, this is a similar seasonal-

ity to that in the NH, indicating OH control as well. During austral spring, there are slightly enhanced C_2H_2 amounts of 50–80 pptv between 30 and 50° S, which reflects the southward transport of air masses polluted by southern hemispheric biomass burning. Due to its relatively short lifetime,

the southward expansion of enhanced C_2H_2 to Antarctic latitudes in austral summer is not observed.

4.1.4 Ethane (C_2H_6)

Similarly to C_2H_2, much higher C_2H_6 amounts were observed in the northern extratropics than in the tropics and at southern latitudes (Fig. 4, right column). The annual cycle at northern middle and high latitudes with maximum VMRs of up to more than 1000 pptv in winter and spring and with minimum values around 700 pptv in late summer and fall shows that these variations are also not dominated by biomass burning. Like for C_2H_2, the annual cycle of the OH radical is the dominant reason for the C_2H_6 maximum in the NH during winter (Rudolph, 1995; Xiao et al., 2008; Helmig et al., 2015). For the same reasons as outlined above, the northern extratropical C_2H_6 distribution shows longitudinal variations similar to C_2H_2 during fall and winter.

The tropical and subtropical C_2H_6 distribution exhibits similarities to those of HCN and C_2H_2. There are also moderately enhanced C_2H_6 amounts of ~ 500 pptv above western and northern Africa in spring, inside the AMA in summer, and in the SH in austral spring, indicating the release of C_2H_6 from biomass burning. However, during boreal summer, C_2H_6 amounts of 500–600 pptv are visible around Central America, above the southeastern United States, and above the North Atlantic. These enhancements, which are not correlated with HCN and C_2H_2, become more evident further below the tropopause. Therefore, they are presented at 10 km altitude in the Appendix in comparison with the other trace gases.

The lowest C_2H_6 VMRs of 200 pptv or less were observed at southern midlatitudes and high latitudes during austral summer (DJF) and fall (MAM). In austral winter (JJA), the amounts increase slightly at southern midlatitudes, which might also be caused by the minimum in the OH cycle. As a result of biomass burning in the southern tropics and subtropics during austral spring (SON), the C_2H_6 amounts accumulate somewhat more at southern midlatitudes and even slightly increase at high latitudes. Contrarily to HCN, there is no further C_2H_6 enhancement but rather a reduction at high southern latitudes in austral summer (DJF), which probably is due to its shorter lifetime.

4.1.5 Peroxyacetyl nitrate (PAN)

By far the highest PAN amounts were observed at northern middle and high latitudes during boreal summer (Fig. 5c), with maximum amounts of 450 pptv above northeastern Europe and Siberia. The lowest northern hemispheric PAN VMRs of 70–130 pptv were measured during boreal winter. The spatial distribution and seasonal variation in northern extratropical PAN exhibit similarities to HCN, indicating biomass burning as a potential source. However, according to Fischer et al. (2014), PAN production in the northern

extratropics is driven by anthropogenic and biogenic activities during spring and dominated by biogenic species during summer, with isoprene as major precursor (37 %). Other non-methane volatile organic compounds listed by Fischer et al. (2014), which contribute to PAN formation, are acetone and C_2H_6. We will further investigate the origin of northern hemispheric PAN in Sect. 4.3. Similarly to C_2H_6, enhanced PAN amounts were also measured above the northern Atlantic between the east coast of the United States and Europe.

The tropical and subtropical PAN distribution is spatially well correlated with HCN during all seasons, pointing to biomass burning as an important source of upper-tropospheric PAN in these regions. During the southern hemispheric fire season in austral spring (SON), PAN VMRs of up to 240 pptv were observed between South America and southern Africa. In this season, enhanced PAN VMRs of up to 150 pptv also cover the latitude band 30–50° S, reflecting the southward expansion of air masses polluted by biomass burning. Similarly to C_2H_2 and C_2H_6, there is no further expansion of enhanced PAN amounts to high southern latitudes in austral summer (DJF). During the other seasons, the PAN amounts at southern hemispheric middle and high latitudes are very low.

4.1.6 Formic acid (HCOOH)

The highest HCOOH VMRs were observed at northern middle and high latitudes during summer, with maxima of 180 pptv above Siberia and the Canadian Arctic (Fig. 5d). During winter, the HCOOH amounts in the northern extratropics decline to 50–70 pptv (Fig. 5h). The correlation of the annual variation in northern hemispheric HCOOH both with the vegetation and with the HCN cycles points to biogenic sources and to release by biomass burning. This is further investigated in Sect. 4.3.2.

The spatial distribution of enhanced HCOOH above tropical and subtropical Africa is in good agreement with enhanced HCN during all seasons. The highest HCOOH amounts in the southern tropics and midlatitudes with maximum values of up to 160 pptv above tropical South America and Africa were observed in austral spring (Fig. 5f). Please note that the HCOOH distributions during austral spring and summer are displayed at an altitude of 5 km instead of 3 km below the tropopause because some features of tropical HCOOH become better visible at this level. During this season, enhanced HCOOH coincides well with the HCN plume extending from Brazil over southern Africa and the southern Indian and Pacific oceans. The good spatial correlation with HCN in these regions is a strong indication for a significant contribution from biomass burning to upper-tropospheric HCOOH during austral spring.

Due to practically year-round biomass burning signatures over Africa, a clear detection of the biogenic release of HCOOH in this region is difficult in the seasonal composites presented in Fig. 5. The separation between biogenic
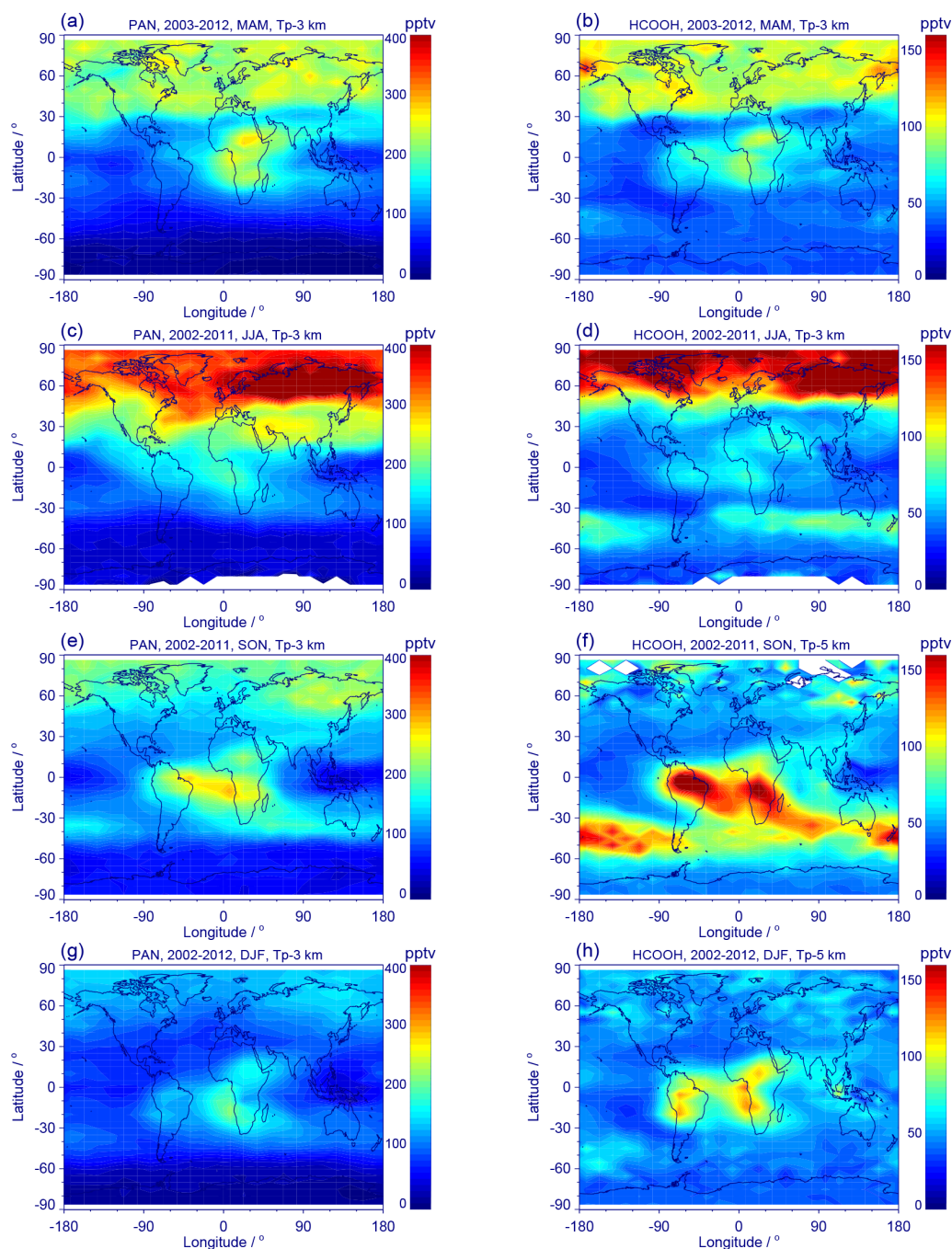
Figure 5. Global PAN distribution measured by MIPAS at 3 km below the tropopause during **(a)** March to May, **(c)** June to August, **(e)** September to November, and **(g)** December to February, as well as global HCOOH distribution measured by MIPAS at 3 km below the tropopause during **(b)** March to May, **(d)** June to August, **(f)** September to November, and **(h)** December to February. The distributions are averaged over the time period 2002 to 2012. Note that the HCOOH distributions of September to November and December to February are at 5 km below the tropopause.

and biomass burning sources of HCOOH is somewhat easier above tropical South America. Here, local maxima of enhanced HCOOH are visible during austral spring and summer (Fig. 5f and h). In particular, the maxima during December to February are not correlated with HCN, which hints to

direct biogenic emission or generation from other biogenic sources, e.g., isoprene (Keene and Galloway, 1988). Rather, a clear indication of biogenic HCOOH release in the Amazon region during July and August can be seen in Figs. A2 and A3 in the Appendix.

Besides in austral spring, at least slightly enhanced HCOOH amounts were also observed in the latitude band 30–60° S in all other seasons. Differently to the period September to November, these enhancements are not so well correlated with HCN, which hints to a strong contribution from biogenic sources. Relevant source regions are tropical South America and tropical Africa. Figure S7 in the Supplement shows how, for example, during August 2010, air masses from the boundary layer above Brazil are transported into the UT in this latitude band. According to Franco et al. (2020, their Fig. 4), the Amazon rainforest in particular is a strong source of HCOOH precursors, such as isoprene and monoterpenes. Their fluxes strongly increase during austral winter and peak in austral spring around September. At southern high latitudes, very low HCOOH amounts were measured during most of the year, with a slight increase up to about 70 pptv during austral spring.

4.2 Monthly volume mixing ratios in different latitude bands

Figure 6 shows monthly averaged VMRs observed by MIPAS in 10°-wide latitude bands at 3 km below the tropopause. As already shown in Fig. 2, HCN exhibits two maxima of about equal strength, one located in the Northern Hemisphere and the other in the Southern Hemisphere (Fig. 6a). Northern hemispheric HCN peaks in May at midlatitudes and in August at high latitudes, reflecting the northward progression of biomass burning. The enhanced HCN amounts observed from May to August between 10 and 40° N are caused by the northern African plume and by the accumulation of HCN in the AMA starting in June. In the southern hemispheric tropics and midlatitudes, strongly elevated HCN amounts were observed between September and December, with maxima during October–November. Thereafter, the HCN amounts continuously decrease during austral winter and spring. At high southern latitudes, maximum HCN amounts were measured in December, which is due to the time required for southward transport from the biomass burning regions in the SH. Compared to southern hemispheric lower latitudes, the decrease begins 1 month later. In the northern extratropics, the lowest HCN VMRs were observed in December, in the northern tropics during January–February, in the southern tropics during March–April, and at southern middle to high latitudes during May–June.

At northern middle and high latitudes, the monthly variation in CO (Fig. 6b) exhibits similarities to HCN, but the CO maximum in summer is less distinct. Instead, high CO amounts were observed during most of the year, indicating release by other anthropogenic sources in addition to biomass burning. Enhanced CO was also measured in the northern tropics in spring and in the northern subtropics in summer. The CO maximum in October–November in the southern tropics is well correlated with HCN, which hints at release by biomass burning. Southward expansion of polluted air

masses is visible in slightly enhanced CO at high southern latitudes between September and November. However, contrarily to HCN, there is already a strong decrease at southern middle and high latitudes in December.

In the northern extratropics, strong maxima of C_2H_2 and C_2H_6 were observed in February–March, and minima were observed in summer at high latitudes and in fall at midlatitudes (Fig. 6c and d). Due to its shorter lifetime under sunlit conditions, the decrease in C_2H_2 is considerably stronger than that of C_2H_6. Ethane also exhibits enhanced VMRs in the northern tropics in spring and in the northern subtropics in summer. The more localized C_2H_2 maxima in these regions shown in Fig. 4 are hardly visible here due to zonal averaging. Due to their shorter lifetimes, the C_2H_6 and C_2H_2 enhancements in southern hemispheric spring are temporally more restricted than those of HCN, with maxima in September–October and a strong decrease in December.

In the northern extratropics, both PAN and HCOOH exhibit maxima in summer and minima in winter (Fig. 6e and f). This similarity to HCN points to release by biomass burning. However, as mentioned above, other anthropogenic and biogenic sources are possible as well. We try to obtain more information on their origin in the correlation analysis in Sect. 4.3. In the representation chosen here, HCOOH enhancements are hardly visible in the northern tropics and subtropics. In the southern tropics and at southern midlatitudes, maximum PAN amounts were observed in October and November, which is in phase with the HCN cycle. This is a strong indication for the release of PAN by biomass burning. Maximum southern hemispheric HCOOH amounts were measured during September to October. At southern midlatitudes, HCOOH already increases considerably in August, i.e., 1 month before HCN. As mentioned above, this points to the biogenic release of HCOOH, which, in the following months, becomes superposed by biomass burning. While enhanced PAN amounts were observed up to 50° S, enhanced HCOOH extends further southward up to 60–70° S.

4.3 Global tracer–tracer correlation and regression analysis

In the following, we discuss the results of correlation and regression analyses between the biomass burning tracer HCN and the other pollutants to obtain a more quantitative assessment of their sources.

4.3.1 Monthly correlation coefficients in different latitude bands

Figure 7 shows Pearson correlation coefficients r obtained for monthly composites of single-scan MIPAS data in 5°-wide latitude bands at 3 km (50° S–50° N) and at 2 km (higher latitudes) below the tropopause. The lower distance to the tropopause at high latitudes was chosen to ensure a suf-
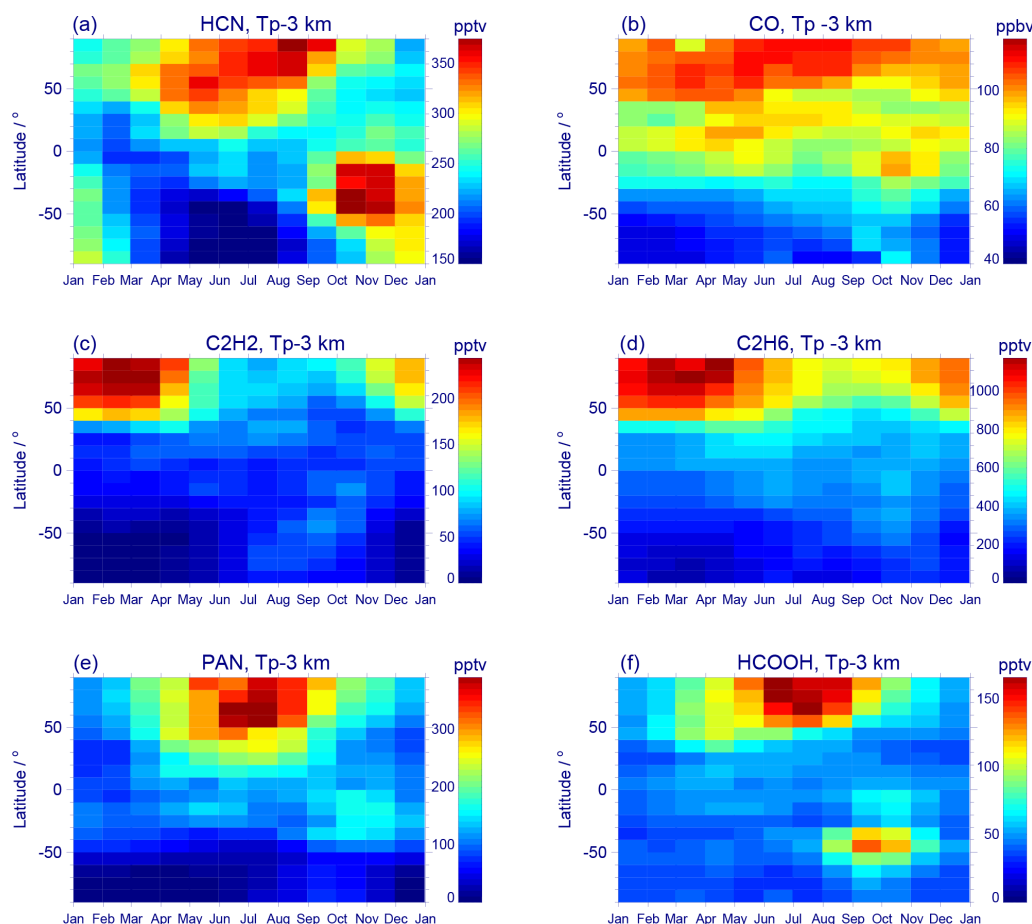
Figure 6. Time series of monthly composites of **(a)** HCN, **(b)** CO, **(c)** C_2H_2, **(d)** C_2H_6, **(e)** PAN, and **(f)** HCOOH VMRs in $10°$-wide latitude bands at an altitude of 3 km below the tropopause. The datasets are averaged over the time period 2002–2012.

ficiently high number of data points for the correlation analysis in these regions.

The pollutants C_2H_2 and PAN exhibit the highest correlations with HCN (Fig. 7b and d). In both cases, correlation coefficients between $r = 0.7$ and $r = 0.85$ were obtained for observations between low southern and northern midlatitudes during boreal spring and between the Equator and southern midlatitudes during austral spring. This is a strong indication that at these times, like for HCN, biomass burning was the major source of enhanced C_2H_2 and PAN in these areas. Beyond that, high PAN–HCN correlations were additionally observed at low latitudes in February, June, and November to December. High C_2H_2–HCN correlation coefficients also prevail at northern middle and high latitudes during boreal summer and early fall, pointing to the release of C_2H_2 by biomass burning as well. From October to March, the C_2H_2 and HCN amounts at northern high latitudes are uncorrelated, confirming the dominant influence of the OH cycle and of biofuel burning on the C_2H_2 amounts in these regions during winter. North of $50°$ N, PAN and HCN amounts are not correlated or are only weakly correlated between

November and June, indicating that the strong PAN increase in the northern extratropics during spring and early summer is not dominated by biomass burning but has anthropogenic or biogenic sources. This observation agrees with model results of Fischer et al. (2014), who identify anthropogenic and biogenic activities as major sources of northern extratropical PAN during boreal spring and summer (see Sect. 4.1.5). The increasingly higher correlation coefficients at northern middle and high latitudes during July to September hint at growing contributions from boreal fires in late summer.

The correlations of CO, C_2H_6, and HCOOH with HCN are generally weaker (Fig. 7a, c, and e). However, they are also characterized by maxima at southern tropics to midlatitudes during austral spring (r between 0.5 and 0.7) and by somewhat weaker maxima in the northern subtropics and midlatitudes during boreal spring. Moderately high correlations ($r = 0.5$–0.65) at northern midlatitudes and high latitudes during boreal summer point to biomass burning as a common source as well. Compared to C_2H_2 and PAN, the lower correlations at low latitudes indicate a larger contri-
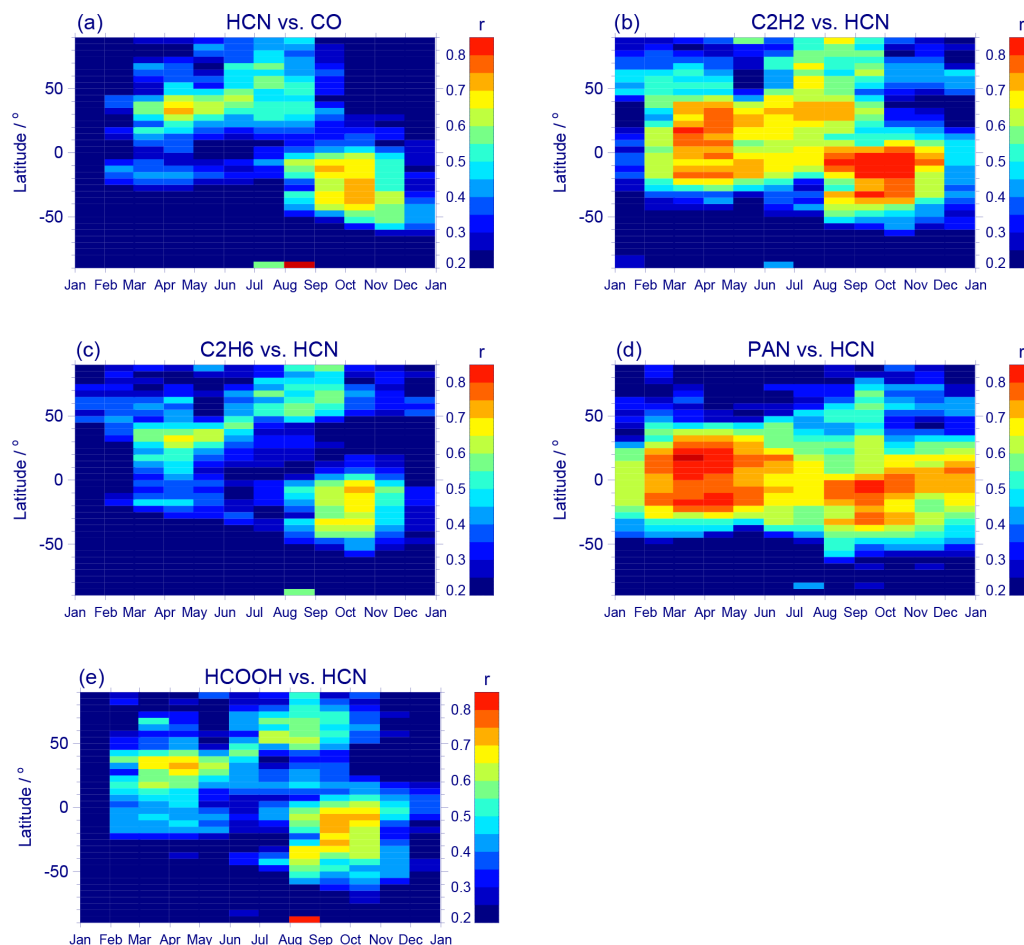
Figure 7. Monthly composites of Pearson correlation coefficients r resulting from correlation analyses between MIPAS measurements in 5°-wide latitude bands, between 50° S and 50° N at 3 km, and at higher latitudes at 2 km below the tropopause. **(a)** HCN versus CO, **(b)** C_2H_2 versus HCN, **(c)** C_2H_6 versus HCN, **(d)** PAN versus HCN, **(e)** HCOOH versus HCN. Values lower than 0.2 or higher than 0.9 are also labeled in dark blue or dark red, respectively.

bution of other anthropogenic or biogenic sources to the enhanced CO, C_2H_6, and HCOOH observed there.

4.3.2 Correlation coefficients and enhancement ratios in latitude–longitude bins

We now discuss correlation coefficients and enhancement ratios (ERs) in 5° × 15° latitude–longitude bins for selected monthly composites at 3 km (50° S–50° N) and 2 km (higher latitudes) below the tropopause. As an example of the underlying data, scatter plots of C_2H_2 versus HCN for a bin above southern Africa are presented in Fig. S9 in the Supplement.

Enhancement ratios are used to gain information on the type of fuel burned by comparison of remotely measured data with emission ratios determined directly at the source. The ER of species X is defined as the difference ΔX between its mixing ratio in a certain plume and its mixing ratio in background air, divided by the difference ΔY of a widely non-reactive co-emitted tracer such as CO or CO_2 (Lefer et

al., 1994; Hobbs et al., 2003; Akagi et al., 2011). In contrast, emission ratios are measured directly at the sources. They can be derived from emission factors (emitted compound among biomass burned in $g\,kg^{-1}$) determined for various trace species by burning under laboratory conditions or by measurements close to open or domestic fires. Measurements of emission factors for burning of various types of vegetation were performed, for example, by Bertschi et al. (2003) and Yokelson et al. (2003, 2008, 2009) and by other authors referenced therein. Comprehensive compilations were given by Andreae and Merlet (2001), Akagi et al. (2011), and Andreae (2019). In comparing ERs with emission ratios, it has to be considered that both can differ from each other due to plume aging (faster depletion of shorter-lived species).

We calculated monthly $\Delta HCN/\Delta CO$ and $\Delta X/\Delta HCN$ (X = C_2H_2, C_2H_6, PAN, or HCOOH) enhancement ratios by linear Deming regression analysis (Deming, 1943). This method of regression analysis, which is equivalent to the maximum likelihood estimation of the slope of the regres-

sion, was chosen because of uncertainties of different magnitude both in HCN and in the other pollutants, and it was implemented as described in Mikkonen et al. (2019). In this regression model, the uncertainties σ_1 and σ_2 of both pollutants are taken into account by introducing a parameter $\lambda = \sigma_1^{-2} \times \sigma_2^2$, which we determined from the ESDs given in Table 2 as $\lambda = \text{ESD}_1^{-2} \times \text{ESD}_2^2$. After averaging over the two height levels in Table 2, the following global λ values were applied: $\Delta\text{HCN}/\Delta\text{CO}$: 4.42×10^{-6}, $\Delta\text{C}_2\text{H}_2/\Delta\text{HCN}$: 0.35, $\Delta\text{C}_2\text{H}_6/\Delta\text{HCN}$: 20.01, $\Delta\text{PAN}/\Delta\text{HCN}$: 0.63, and $\Delta\text{HCOOH}/\Delta\text{HCN}$: 0.75. In the case of equal error variances for both variables, Deming regression simplifies to orthogonal regression. In the following, all enhancement ratios are given in units of $\text{pptv}\,\text{pptv}^{-1}$.

We compare MIPAS ERs with values obtained from ACE-FTS observations of individual plumes and with emission ratios for the burning of different types of vegetation (Table 3), derived from emission factors given in the most recent compilation of Andreae (2019). The values in parentheses in Table 3 show that the standard deviation or natural variation of the emission factors and consequently of the emission ratios generally is larger than 50 % or even 100 % for each type of fuel. These variations are mostly larger than the differences between the emission ratios for the fire types to be considered in a certain global region. One exception is the emission ratio for peat fires, which, compared to other types of biomass burning, is very high for $\Delta\text{HCN}/\Delta\text{CO}$ and very low for all other emission ratios contained in Table 3. The reason is the high HCN emission factor for this type of smoldering combustion. Another exception is the high $\Delta\text{C}_2\text{H}_2/\Delta\text{HCN}$ emission factor for biofuel burning. Furthermore, the $\Delta\text{C}_2\text{H}_6/\Delta\text{HCN}$ and $\Delta\text{HCOOH}/\Delta\text{HCN}$ emission factors for savanna burning are considerably lower than those for the other types of burning (tropical forest, agricultural residues, biofuel) in tropical or subtropical regions.

Because of the different lifetimes of the pollutants, the calculated $\Delta\text{HCN}/\Delta\text{CO}$ enhancement ratios might potentially be higher than the respective emission ratios observed directly at the fires, while the $\Delta X/\Delta\text{HCN}$ enhancement ratios might be lower. On the other hand, $\Delta\text{HCOOH}/\Delta\text{HCN}$ and $\Delta\text{PAN}/\Delta\text{HCN}$ might also become higher than the emission ratios due to post-emission processing. Furthermore, the different vertical resolutions (VRs) of the correlated gases (see Table 2) have to be considered. Fortunately, the VRs of HCN and CO are rather similar at 2–3 km below the tropopause, i.e., at ~ 14 km in the tropics and at ~ 8 km at higher latitudes. Except for tropical C_2H_6, the VRs of the other pollutants are clearly different from the one of HCN. However, degradation of a sample of C_2H_2 profiles of 154 orbits to the height resolution of HCN on average resulted in about 5 % lower VMRs in the southern tropics and 10 % lower VMRs at northern middle and high latitudes, which would lead to 5 %–10 % lower ERs only. Due to these caveats, comparison of the enhancement ratios presented in the following with

Table 3. Upper section: emission factors (g kg^{-1}) for species emitted from different types of biomass burning as given by Andreae (2019). The values in parentheses are the standard deviations between different measurements. Lower section: corresponding emission ratios (pptv pptv^{-1}) with standard deviations, calculated by error propagation, in parentheses. The ratios were calculated under consideration of the molar mass ratios.

Species	Savanna/ grassland	Tropical forest	Temperate forest	Boreal forest	Peat fires	Agric. residues	Biofuels w/o dung	Dung
CO	69(20)	104(39)	113(50)	121(47)	260(23)	76(55)	83(29)	89(42)
HCN	0.44(0.26)	0.44(0.21)	0.64(0.39)	0.53(0.30)	4.4(1.2)	0.42(0.18)	0.39(0.17)	1.27(0.73)
C_2H_2	0.31(0.29)	0.35(0.39)	0.31(0.09)	0.28(0.13)	0.11(0.05)	0.27(0.24)	0.68(0.37)	0.68(0.41)
C_2H_6	0.42(0.32)	0.88(0.23)	0.69(0.56)	0.97(0.37)	1.85(0.35)	0.79(0.62)	0.63(0.61)	1.28(0.70)
HCOOH	0.21(0.13)	0.49(0.28)	0.91(1.18)	1.04(0.89)	0.29(0.14)	0.56(0.45)	0.23(0.22)	0.39(0.05)
PAN	–	–	–	–	–	–	–	–
$\Delta\text{HCN}/\Delta\text{CO}$	0.0066(0.0044)	0.0044(0.0027)	0.0059(0.0044)	0.0045(0.0031)	0.0175(0.0050)	0.0057(0.0048)	0.0049(0.0027)	0.0150(0.011)
$\Delta\text{C}_2\text{H}_2/\Delta\text{HCN}$	0.73(0.81)	0.83(1.00)	0.50(0.34)	0.55(0.40)	0.03(0.01)	0.67(0.66)	1.81(1.26)	0.56(0.46)
$\Delta\text{C}_2\text{H}_6/\Delta\text{HCN}$	0.86(0.83)	1.80(0.98)	0.97(0.98)	1.65(1.12)	0.38(0.13)	1.69(1.51)	1.45(1.54)	0.91(0.72)
$\Delta\text{HCOOH}/\Delta\text{HCN}$	0.28(0.24)	0.65(0.49)	0.83(1.20)	1.15(1.18)	0.04(0.02)	0.78(0.71)	0.35(0.36)	0.18(0.11)
$\Delta\text{PAN}/\Delta\text{HCN}$	–	–	–	0.9–2.75[a]	–	–	–	–

[a] Derived from values in Tereszchuk et al. (2013b).
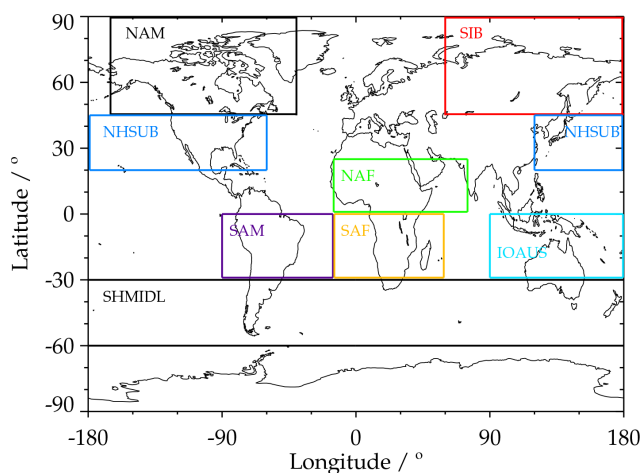
Figure 8. Global regions for which the mean enhancement ratios shown in Table 4 and discussed in Sect. 4.3.2 were calculated. NAM: boreal North America; SIB: Siberia; NHSUB: northern hemispheric subtropics; NAF: northern Africa; SAM: South America; SAF: southern Africa; IOAUS: Indonesia and Australia; SHMIDL: southern hemispheric midlatitudes.

emission ratios has to be performed with caution. However, the consideration of ERs in addition to the correlation coefficients has a synergistic effect: high correlations with HCN in combination with ERs in the range of the listed emission ratios indicate biomass burning. On the other hand, enhancement ratios far out of the range of possible emission ratios point to other sources of the other pollutants even in the case of a high correlation with HCN.

For statistical reasons, we only show correlation coefficients and ERs for bins with at least 10 data pairs in the following plots. To restrict the presentation to bins with enhanced VMRs of the respective pollutant, further filter criteria are mean bin values of 80 ppbv for CO, 60 pptv for C_2H_2, 300 pptv for C_2H_6, 100 pptv for PAN, and 60 pptv for HCOOH. For comparisons with the emission ratios in Table 3 and enhancement ratios of ACE-FTS, we calculated mean ERs from all bins with correlation coefficients $r > 0.6$ (> 0.55 for CO) in eight different global regions (Fig. 8). For selected months, these ERs are shown in Table 4.

HCN versus CO

Figure 9 shows global distributions of the correlation coefficients (left column) and enhancement ratios (right column) obtained from the correlation analysis between HCN and CO for February, April, July, and October (top to bottom).

During February, moderately strong CO–HCN correlations (around $r = 0.6$) were observed above northeastern Africa, the Middle East, the southern tropical Atlantic, and the eastern North Pacific around 40° N, indicating potential common release of HCN and CO by biomass burning into these air masses. The respective mean

$\Delta HCN/\Delta CO$ enhancement ratios, calculated for bins with correlation coefficients $r > 0.55$, are $(1.8 \pm 0.3) \times 10^{-3}$ for northern Africa, $(1.9 \pm 0.4) \times 10^{-3}$ for southern Africa, and $(2.7 \pm 0.7) \times 10^{-3}$ for the northern Pacific (see Table 4). The values around Africa are considerably lower than the emission ratio of 6.6×10^{-3} for savanna and grassland fires listed in Table 3, which, according to, for example, Yokelson et al. (2003) and van der Werf et al. (2010, 2017), dominate the fire carbon emissions in Africa. They are also lower than the emission ratios of the other types of fuel possibly burned in these regions, namely tropical forest (4.4×10^{-3}) or agricultural residues (5.7×10^{-3}), listed in Table 3. The same applies for the observations above the eastern Pacific. This hints to additional anthropogenic sources of the observed CO amounts, leading to lower enhancement ratios.

During April, there are strong HCN–CO correlations of up to $r = 0.8$ above the Middle East and in the latitude band 20–50° N between the North Pacific and the North Atlantic, which strongly indicate common release by biomass burning and moderately high correlations around $r = 0.5$ above southern Africa. The mean enhancement ratios above northern and southern Africa have hardly changed and amount to $(1.5 \pm 0.3) \times 10^{-3}$ and $(2.2 \pm 0.8) \times 10^{-3}$, respectively. The mean ER above the northern Pacific, the United States, and the northern Atlantic is $(2.9 \pm 0.6) \times 10^{-3}$, which is somewhat closer to the emission ratios in Table 3. Furthermore, this value is in very good agreement with the enhancement ratio of 2.6×10^{-3} (all data) or 3.4×10^{-3} (filtered for low ΔC_2Cl_4) for measurements in the free troposphere above the northern Pacific during spring 2001, reported by Singh et al. (2003).

The month of July is characterized by high correlations above eastern Siberia and Alaska but also scattered above Canada and the Arctic, pointing to the common release of HCN and CO by boreal fires. The mean enhancement ratio for bins with $r > 0.55$ is $(2.7 \pm 0.7) \times 10^{-3}$ for North America and $(3.0 \pm 1.2) \times 10^{-3}$ for Siberia, which corresponds very well with the values for boreal fires given in Tereszchuk et al. (2013a). These authors obtained ERs of $(2.0 \pm 0.9) \times 10^{-3}$–$(2.5 \pm 1.2) \times 10^{-3}$ for North American and of $(2.6 \pm 0.2) \times 10^{-3}$–$(3.0 \pm 1.1) \times 10^{-3}$ for Siberian biomass burning plumes aged between 0 and 7 d from ACE-FTS measurements during the BORTAS campaign from 12 July to 3 August 2011. Based on FTIR measurements of ground-based column amounts at Eureka and Thule during 2008–2012, Viatte et al. (2015) determined average $\Delta HCN/\Delta CO$ ERs of $(3.3 \pm 0.9) \times 10^{-3}$ and $(4.3 \pm 2.5) \times 10^{-3}$, respectively, for mostly boreal forest fires. Both the ERs determined from MIPAS and ACE-FTS measurements are lower than the emission ratio of $(4.5 \pm 3.1) \times 10^{-3}$ for boreal forest fires derived from the values given in Andreae (2019) (Table 3) but well within its standard deviation. On the other hand, they are higher than the value of 1.5×10^{-3} derived from the emission factors for extratropical forest given in Andreae and Merlet (2001).

Table 4. Mean enhancement ratios (pptv pptv^{-1}) calculated from MIPAS measurements in different global regions (see Fig. 8), presented for a minimum number of at least four bins. The thresholds for inclusion of individual $5° \times 15°$ bins for calculation of regional mean ERs are 80 ppbv for CO, 60 pptv for C_2H_2, 300 pptv for C_2H_6, 100 pptv for PAN, and 60 pptv for HCOOH. Further criteria: number of points per bin ≥ 10 and correlation coefficient $r \geq 0.6$ ($r \geq 0.55$ for $\Delta HCN/\Delta CO$). The numbers in parentheses indicate the 1-σ standard deviations of the bin averages. The λ values used for Deming regression analysis are 4.42×10^{-6} for $\Delta HCN/\Delta CO$, 0.35 for $\Delta C_2H_2/\Delta HCN$, 20 for $\Delta C_2H_6/\Delta HCN$, 0.63 for $\Delta PAN/\Delta HCN$, and 0.75 for $\Delta HCOOH/\Delta HCN$.

Region	NAM	SIB	NHSUB	NAF	SAM	SAF	IOAUS	SHMIDL
$\Delta HCN/\Delta CO$								
Feb	–	–	0.0027(0.0007)	0.0018(0.0003)	–	0.0019(0.0004)	–	–
Apr	0.0024(0.0007)	0.0033(0.0012)	0.0029(0.0006)	0.0015(0.0003)	–	0.0022(0.0008)	–	–
Jul	0.0027(0.0007)	0.0030(0.0012)	0.0021(0.0007)	–	–	0.0022(0.0002)	–	–
Aug	0.0044(0.0015)	0.0043(0.0022)	0.0024(0.0008)	–	–	0.0030(0.0006)	–	–
Oct	–	0.0039(0.0011)	–	0.0040(0.0021)	0.0046(0.0014)	0.0051(0.0009)	0.0065(0.0011)	0.0069(0.0017)
$\Delta C_2H_2/\Delta HCN$								
Feb	1.98(0.32)	–	1.83(0.39)	0.81(0.19)	–	0.94(0.18)	–	–
Apr	1.57(0.49)	1.45(0.32)	0.98(0.30)	0.61(0.10)	–	0.92(0.32)	–	–
Jul	0.75(0.24)	0.88(0.31)	1.13(0.29)	1.04(0.22)	–	0.94(0.22)	–	–
Aug	0.55(0.21)	0.56(0.26)	1.20(0.34)	1.06(0.25)	0.64(0.09)	0.75(0.16)	–	0.58(0.16)
Sep	0.55(0.19)	0.56(0.34)	1.54(0.15)	1.05(0.44)	0.43(0.11)	0.56(0.19)	–	0.46(0.10)
Oct	1.31(0.42)	–	–	0.45(0.19)	0.34(0.06)	0.33(0.08)	0.20(0.08)	0.32(0.07)
$\Delta C_2H_6/\Delta HCN$								
Feb	6.06(1.97)	–	5.87(2.85)	1.83(0.39)	–	–	–	–
Apr	6.09(3.33)	6.67(2.23)	2.94(1.96)	1.72(0.28)	–	–	–	–
Jul	3.81(1.27)	3.18(1.02)	–	–	–	–	–	–
Aug	2.37(0.72)	2.37(0.83)	2.49(1.67)	–	–	1.04(0.19)	–	0.97(0.09)
Sep	3.05(1.06)	2.49(0.68)	–	–	1.08(0.22)	1.08(0.52)	–	1.08(0.20)
Oct	4.74(1.28)	–	–	1.14(0.34)	0.93(0.11)	0.86(0.09)	0.64(0.22)	0.95(0.13)
$\Delta PAN/\Delta HCN$								
Feb	1.62(0.27)	–	1.22(0.22)	1.78(0.28)	1.62(0.33)	1.69(0.26)	–	1.63(0.21)
Apr	2.71(1.16)	–	1.62(0.28)	2.03(0.74)	1.27(0.20)	2.12(0.77)	1.46(0.32)	1.70(0.39)
Jul	3.06(0.78)	2.77(0.89)	2.66(0.91)	1.93(0.54)	1.09(0.09)	1.16(0.17)	–	–
Aug	2.24(0.70)	2.64(0.88)	2.39(0.76)	1.85(0.57)	1.65(0.44)	1.16(0.18)	–	1.26(0.24)
Oct	2.36(0.69)	2.51(0.73)	1.48(0.57)	1.55(0.37)	1.09(0.27)	1.00(0.28)	0.61(0.20)	0.76(0.16)
$\Delta HCOOH/\Delta HCN$								
Feb	–	–	1.05(0.28)	0.77(0.28)	–	0.65(0.16)	–	–
Apr	0.76(0.31)	1.06(0.33)	0.77(0.27)	0.57(0.15)	–	–	–	–
Jul	1.87(0.55)	1.53(0.38)	–	–	–	–	–	–
Aug	1.05(0.66)	1.26(0.45)	0.90(0.16)	–	1.19(0.26)	0.92(0.79)	–	1.90(0.78)
Sep	0.85(0.41)	1.14(0.79)	–	–	0.82(0.27)	0.60(0.27)	–	1.16(0.45)
Oct	0.91(0.19)	0.96(0.54)	–	–	0.54(0.18)	0.40(0.11)	0.41(0.35)	0.73(0.25)
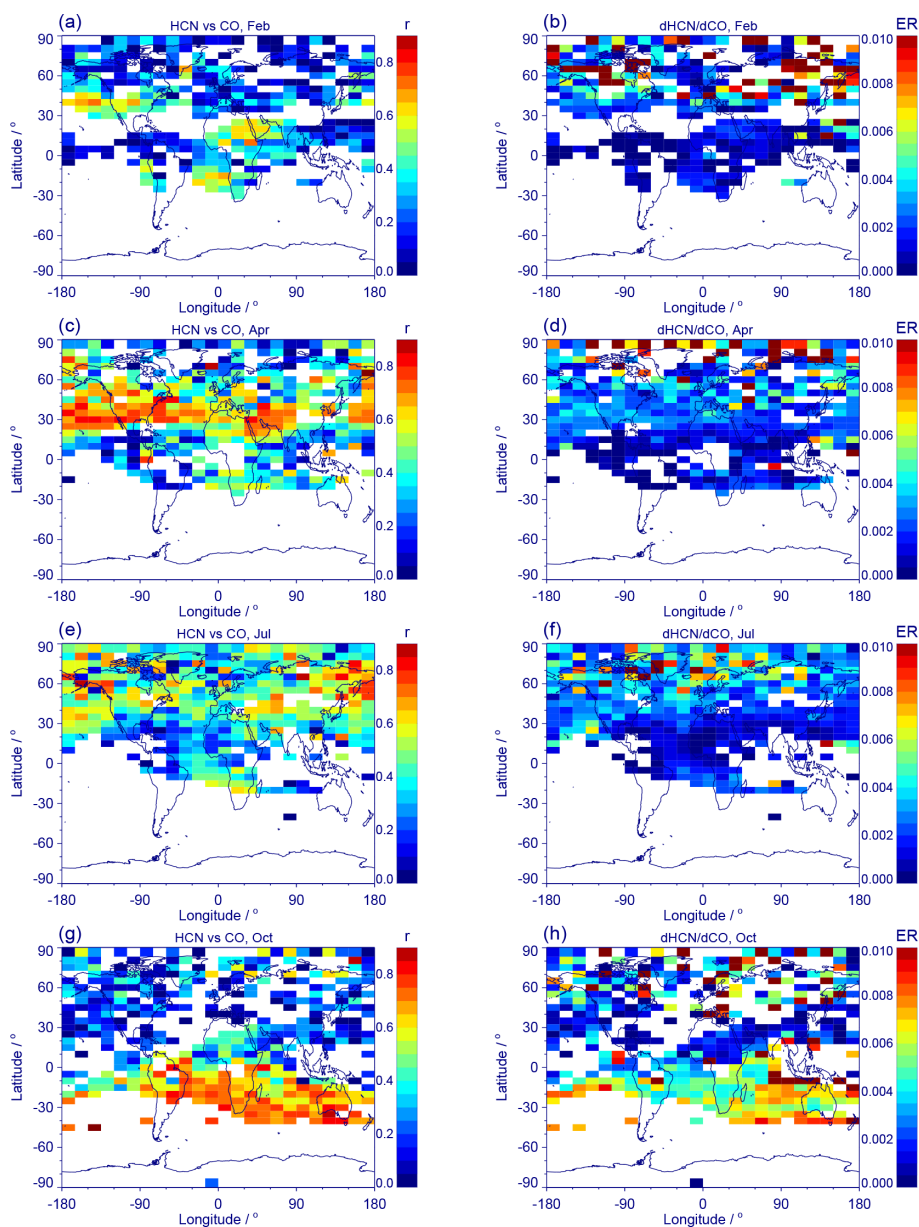
Figure 9. Global distribution of correlation coefficients r between MIPAS measurements of HCN and CO in the upper troposphere for **(a)** February, **(c)** April, **(e)** July, and **(g)** October, as well as the respective ΔHCN / ΔCO enhancement ratios (ERs) in pptv pptv^{-1} for **(b)** February, **(d)** April, **(f)** July, and **(h)** October. The displayed altitude is 3 km below the tropopause in the latitude region 50° S to 50° N and 2 km below the tropopause at higher latitudes. White areas are regions with correlation coefficients or enhancement ratios lower than zero, with CO VMRs lower than 80 ppbv, or with bins containing fewer than 10 values. The bin size is 5° × 15° latitude by longitude. The distributions are monthly composites of the time period 2002 to 2012.

In any case, as already stated by Tereszchuk et al. (2011), these observations indicate that the HCN/CO emission ratio of $(1.24 \pm 8.0) \times 10^{-2}$ derived from the emission factors in Akagi et al. (2011) is too high. The North American and Siberian ERs for August also shown in Table 4 are higher, namely $(4.4 \pm 1.5) \times 10^{-3}$ and $(4.3 \pm 2.2) \times 10^{-3}$, which agrees very well with the values given by Andreae (2019). Like in February and April, there is an area of moder-

ately high correlations above southern Africa and the southern tropical Atlantic, with a mean ER of $(2.2 \pm 0.2) \times 10^{-3}$. Again, this ER is lower than to be expected from the regional types of biomass burning, which points to additional sources of CO. In August, the mean ER increases to $(3.0 \pm 0.6) \times 10^{-3}$, which becomes closer to the emission ratio of 4.4×10^{-3} for tropical forest fires.

The October data show a large area of high correlations up to $r = 0.85$ extending from tropical South America to southern Africa and over wide regions in the southern tropics to midlatitudes, which strongly points to biomass burning as the common source of both pollutants. This is confirmed by the mean ERs of $(5.1 \pm 0.9) \times 10^{-3}$ and $(4.6 \pm 1.4) \times 10^{-3}$ obtained for southern Africa and South America, respectively, which are in good agreement with the emission ratios of 6.6×10^{-3} and 4.4×10^{-3} for savanna and tropical forest fires in Table 3. While the major contribution to pollution in southern Africa is attributed to savanna or woodland fires, pollution in South America approximately in equal parts results from savanna/shrubland fires and from tropical forest fires (van der Werf et al., 2017). There is also good agreement with the enhancement ratios given by Tereszchuk et al. (2011, their Table 1) for ACE-FTS measurements in plumes released from the Congo and the Amazon region, which are $(5.5 \pm 0.2) \times 10^{-3}$ and $(3.6 \pm 0.1) \times 10^{-3}$, respectively. While the $\Delta HCN/\Delta CO$ ERs for savanna and tropical forest fires derived from the emission factors given in Akagi et al. (2011) are nearly identical to those in Table 3 derived from the emission factors in Andreae (2019), the respective values on the basis of the compilation of Andreae and Merlet (2001) are $(0.4 \pm 0.2) \times 10^{-3}$ and 1.5×10^{-3}, which, in comparison to the observed ERs, clearly seem to be too small.

The highest October enhancement ratios of $(6.5 \pm 1.1) \times 10^{-3}$ and $(6.9 \pm 1.7) \times 10^{-3}$ for bins with $r > 0.55$ were obtained for measurements above the tropical Indian Ocean/Indonesia (IOAUS) and above southern hemispheric midlatitudes (SHMIDL), respectively. Figure 9h shows that the high ERs at southern midlatitudes are focused to the eastern Indian Ocean, which is adjacent to the Indonesian/Australian region. The value for the region IOAUS for November (not shown) is even higher, namely $(8.4 \pm 2.4) \times 10^{-3}$. In so-called El Niño years, this area is strongly polluted by biomass burning in Indonesia. Biomass burning in Indonesia is characterized by a high percentage of peatland fires, which nearly completely burn under smoldering conditions (Akagi et al., 2011). For this type of fire, Andreae (2019) specifies large HCN emission factors, which lead to a $\Delta HCN/\Delta CO$ emission ratio of 1.8×10^{-2} (Table 3). Thus we conclude that a significant portion of peatland burning is the reason for the high $\Delta HCN/\Delta CO$ enhancement ratios observed above the eastern Indian Ocean. The measured ERs for the October composite are still considerably lower than the emission ratio derived from the Andreae data because biomass burning in Indonesia is significantly intensified in El Niño years only. During the MIPAS measurement period, there were two strong (2002 and 2006) El Niño years and one minor (2009) El Niño year. In all other years, enhanced HCN and CO amounts over the eastern Indian Ocean were presumably dominated by African or Asian fires with lower HCN emission factors.

As can be seen in Fig. S11 in the Supplement, most of the spatial patterns of high correlation coefficients visible in the composite plots presented here also appear in the single-year distribution of 2008. Furthermore, the single-month ERs are mostly of the same magnitude as the monthly composites.

C_2H_2 versus HCN

High correlations between C_2H_2 and HCN occur in even larger regions than those between HCN and CO, and they are generally stronger, often reaching values of $r = 0.8$ or above (Fig. 10, left column). Again, strong correlations are found above northeastern Africa, the southern tropical Atlantic, and the North Pacific in February and April and at northern middle and high latitudes, above tropical Africa, in the AMA region, and above the southern Indian Ocean in August. In October, there are very high correlations above the southern tropical Atlantic, southern Africa, the Indian Ocean, and Australia. All these features strongly point to biomass burning as a common source of C_2H_2 and HCN.

As already mentioned, the considerably shorter lifetime of C_2H_2 compared to HCN is a potential issue in the interpretation of monthly composites of $\Delta C_2H_2/\Delta HCN$ enhancement ratios. Nevertheless, the mean ER obtained for February for the region above northern tropical Africa and the Middle East is 0.81 ± 0.19 (Fig. 10b), which, especially after a 10 %-subtraction, as discussed above, is in good agreement with the emission ratio for the dominant burning process in northern tropical Africa, namely savanna or grassland fires (0.73). However, the emissions for tropical forest fires (0.83) or burning of agricultural residues (0.67) are not much different. The mean ER of 0.94 ± 0.18 for southern tropical Africa is somewhat higher. A possible reason is the additional release of C_2H_2 from biofuel burning, e.g., cooking fires or domestic heating, with a higher emission ratio of 1.81 (Table 3). In any case, these ERs corroborate the assumption that the low $\Delta HCN/\Delta CO$ ERs observed above Africa during February are caused by additional anthropogenic sources of CO. The average ER for the region with high correlations around $40°$ N above the Pacific and North America is 1.83 ± 0.39. Biofuel burning might also come into consideration for this high value, but, due to the spatial non-uniformity of the correlation coefficients and ERs in this region, we also assume mixing with C_2H_2-rich air masses from further north as a possible contribution.

In April, the area of high C_2H_2–HCN correlations above Africa increased and expanded over southern Asia and the Chinese Sea. Furthermore, there is a uniform region of very high correlations around $30°$ N, covering the North Pacific, the United States, and the North Atlantic. Compared to February, the mean enhancement ratio above northern Africa and southern Asia decreased to 0.61 ± 0.10 and exhibits a general decline towards the east, which is an indication of more aged pollution. The ER obtained above southern Africa did not change much and is 0.92 ± 0.32. The mean ER in the band with high correlations around $30°$ N (NHSUB) is 0.98 ± 0.30. This value is clearly lower than the ER deter-
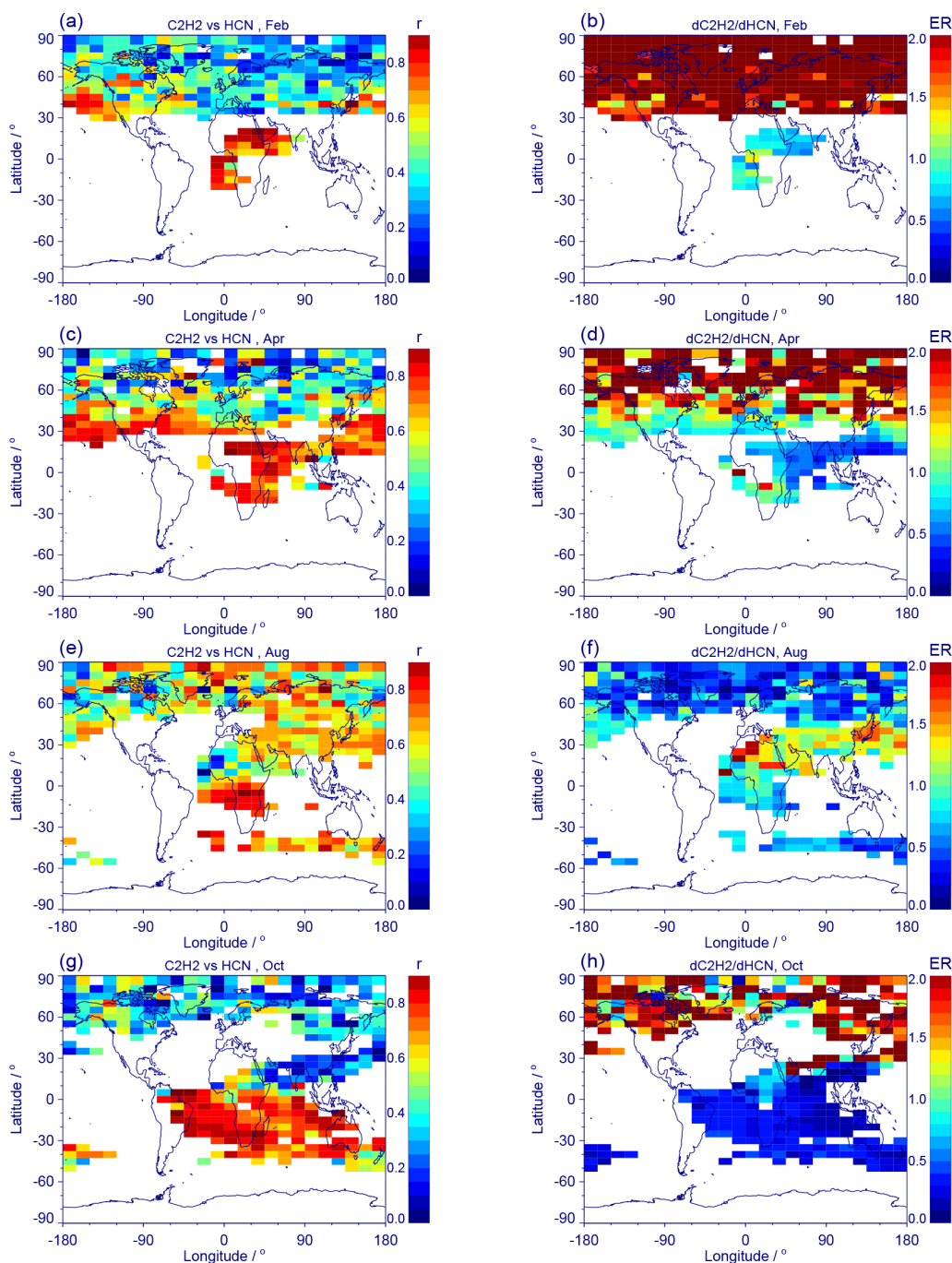
Figure 10. Global distribution of correlation coefficients r between MIPAS measurements of C_2H_2 and HCN in the upper troposphere for **(a)** February, **(c)** April, **(e)** August, and **(g)** October, as well as the respective $\Delta C_2H_2/\Delta HCN$ enhancement ratios (ERs) in pptv pptv^{-1} for **(b)** February, **(d)** April, **(f)** August, and **(h)** October. White areas are regions with correlation coefficients or enhancement ratios lower than zero, with C_2H_2 VMRs lower than 60 pptv, or with bins containing fewer than 10 values. For further details, see Fig. 9.

mined for February and only somewhat above the emission ratios of potential sources, namely tropical forest fires, burning of agricultural residues, and savanna fires. This shows the progressive upper-tropospheric pollution by biomass burning

in tropical eastern Asia and additionally in northern Africa during spring.

In August, the main burning activity in Africa is focused southward of the Equator, and there are very high C_2H_2–HCN correlations above southern tropical Africa and the

tropical Atlantic and in a band around $45°$ S in the Eastern Hemisphere. High to very high correlations were also observed at northern midlatitudes and high latitudes and in the AMA region. All these features indicate the common release of HCN and C_2H_2 by biomass burning. As confirmation, the ERs obtained for southern Africa and South America are 0.75 ± 0.16 and 0.64 ± 0.09, which, differently to the respective $\Delta HCN/\Delta CO$ value for southern Africa, are in good agreement with the emission ratios for savanna and tropical forest fires. The area above northern Africa and the Middle East (NAF), covered by the western part of the AMA, exhibits an ER of 1.06 ± 0.25, pointing to contributions from biofuel burning. The mean ER for the bins of high correlation above North America and Siberia is 0.55 ± 0.21 and 0.56 ± 0.26, respectively, which is in good agreement with the emission ratio for boreal forest fires (0.55 ± 0.40).

In October, high correlations with HCN prevail over large areas in the Southern Hemisphere, which are even stronger than those between HCN and CO. The mean ERs for southern Africa and South America are 0.33 ± 0.08 and 0.34 ± 0.06, respectively, which is much lower than the values of August and the emission ratios coming into question. Presumably, this is an effect of plume aging: in this case, stronger accumulation of HCN during persistent fire activity due to its relatively long lifetime. Compared to South America and southern Africa, the mean ER above the Indian Ocean and Australia is even lower, namely 0.20 ± 0.08, which also points to a contribution from peat fires with an emission ratio of only 0.03 (Table 3).

As an alternative approach, Fig. S10 in the Supplement shows scatter plots of September and October composites of C_2H_2 versus HCN for the whole of southern Africa. The respective ER determined for October is 0.31, which agrees very well with the bin average given above. In Fig. S12 in the Supplement, we present monthly distributions of C_2H_2–HCN correlation coefficients and ERs for the single year 2003. The spatial patterns of high C_2H_2–HCN correlation coefficients are very similar to those of the monthly composites discussed above. Furthermore, the single-month ERs generally agree well with those for monthly composites.

C_2H_6 versus HCN

In most regions and months, the C_2H_6–HCN correlations (Fig. 11, left column) look very similar to those between CO and HCN, reflecting the same regional patterns of biomass burning. Like for HCN versus CO, the correlation coefficients are lower than those between C_2H_2 and HCN, indicating a weaker connection. However, it has to be considered that a certain part of the weaker correlations is due to the large retrieval error of C_2H_6 (see Table 2), which results in a relative retrieval error (divided by VMR) of C_2H_6 that is 2 times larger than that of C_2H_2.

The distribution of $\Delta C_2H_6/\Delta HCN$ enhancement ratios is characterized by values considerably higher than 3 in nearly

the whole northern hemispheric extratropics during February, April, and October (Fig. 11, right column). These ERs are far above the emission ratios for biomass burning (Table 3), and C_2H_6 and HCN are mostly uncorrelated or only moderately well correlated in this region as well. Both findings point to other sources of enhanced C_2H_6 at northern middle and high latitudes during these months, namely accumulation in boreal winter due to the minimum in the OH cycle and anthropogenic activities.

During August, very high ERs above 3 also cover a region extending from the Gulf of Mexico and the central United States above the northern Atlantic towards Europe and from the tropical eastern Pacific to northwestern South America. In these regions, C_2H_6 is also not correlated with HCN. Thus, both the high ERs and the missing correlation indicate that these C_2H_6 enhancements are not caused by biomass burning but by losses of ethane in the oil and gas production and transport (cf. Appendix). During April, i.e., before the onset of the North American monsoon, high ERs were also observed but above northern South America and the tropical eastern Pacific only.

The enhancement ratios in the regions with moderately high (February) and high correlation coefficients (April) are generally much lower. During February and April, mean values for bins with $r > 0.6$ of 1.83 ± 0.39 and 1.72 ± 0.28 were calculated for northern Africa and the Middle East, respectively. These values are clearly higher than the emission ratio for savanna or grassland fires (0.86) but are in good agreement with the emission ratios for tropical forest fires (1.80) or for the burning of agricultural residues (1.69). This either implies a dominance of tropical forest burning instead of savanna fires or additional anthropogenic sources of the enhanced C_2H_6. The ERs in the northern hemispheric subtropics are considerably higher, which points to additional sources and to mixing with air masses from further north. However, like for C_2H_2, the considerable decrease from 5.87 ± 2.85 in February to 2.94 ± 1.96 in April indicates the growing contribution of biomass burning.

In August, the mean ERs for the bins with high correlation coefficients above North America and Siberia are 2.37 ± 0.72 and 2.37 ± 0.83, respectively, which is larger than the emission ratio for boreal fires (1.65). Again, this points to a combination of boreal forest fires and other sources leading to the enhanced C_2H_6 in these regions. The mean ER of bins with high correlations above southern Africa is 1.04 ± 0.19, which is somewhat above the emission ratio for savanna fires (0.86), indicating savanna burning and possibly a certain contribution of tropical forest fires.

The mean ERs for the large area of high southern hemispheric C_2H_6–HCN correlations in October are 0.86 ± 0.09 above southern Africa and 0.93 ± 0.11 above South America, which fit very well to the emission ratio for savanna and grassland burning. This is the dominant biomass burning process in southern Africa during this time of the year. Probably due to the longer lifetime of C_2H_6, the October ER for
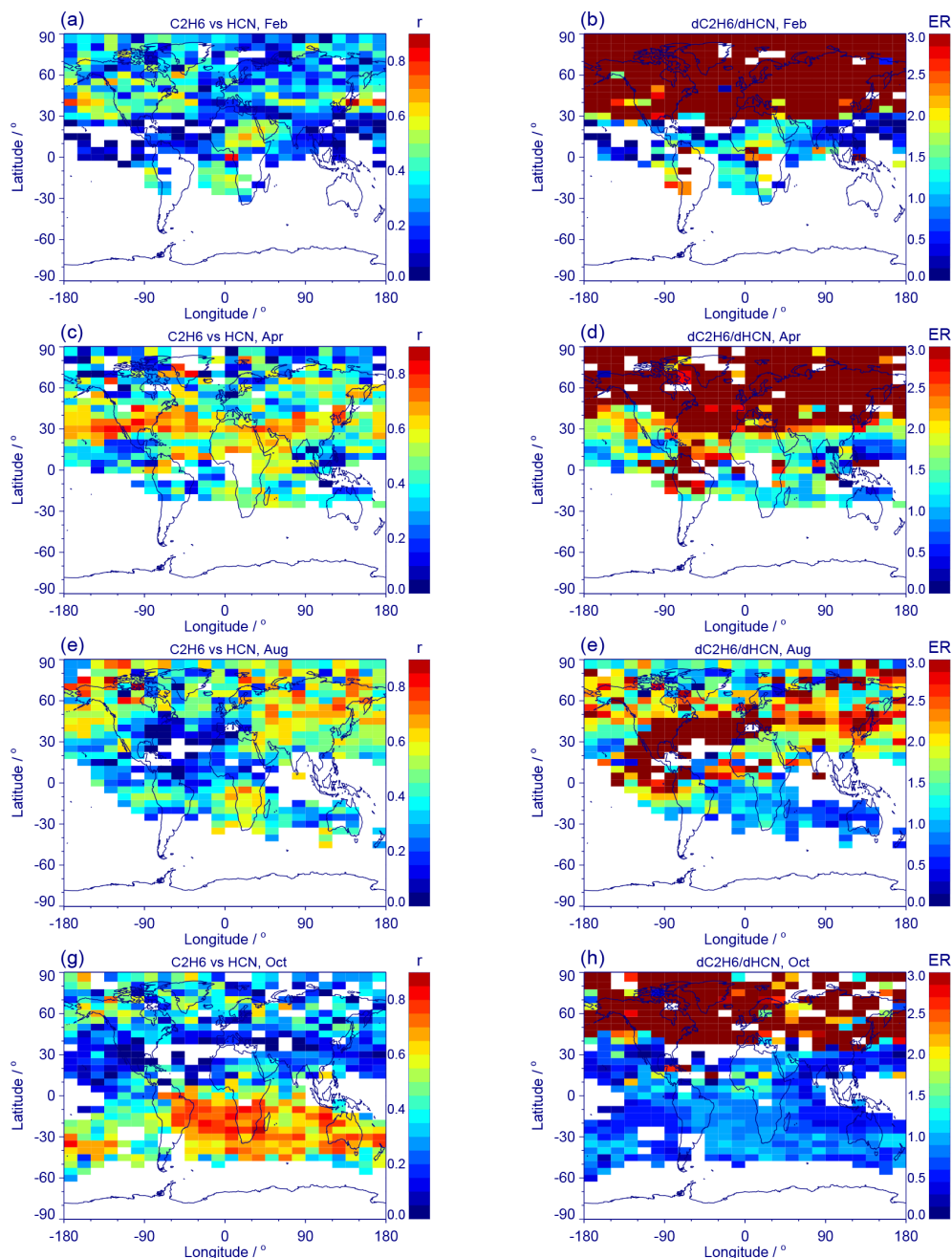
Figure 11. Global distribution of correlation coefficients r between MIPAS measurements of C_2H_6 and HCN in the upper troposphere for **(a)** February, **(c)** April, **(e)** August, and **(g)** October, as well as the respective $\Delta C_2H_6 / \Delta HCN$ enhancement ratios (ERs) in pptv pptv^{-1} for **(b)** February, **(d)** April, **(f)** August, and **(h)** October. White areas are regions with correlation coefficients or enhancement ratios lower than zero, with C_2H_6 VMRs lower than 300 pptv, or with bins containing fewer than 10 values. For further details, see Fig. 9.

southern Africa, contrarily to $\Delta C_2H_2/\Delta HCN$, does not yet reflect plume aging. In South America, savanna burning and tropical forest fires have approximately equal contributions to the annual carbon emissions (van der Werf et al., 2017, their Fig. 9), but this is not reflected in the upper-tropospheric ERs obtained from the MIPAS measurements. The mean ER

above the Indian Ocean and Australia is lower (0.64 ± 0.22), which again points to contributions from peat fires.

PAN versus HCN

The PAN–HCN correlations (Fig. 12, left column) are comparably as strong as those between C_2H_2 and HCN. Dur-

ing February, they are very high above Africa, the Middle East, and the southern tropical Atlantic, as well as in a smaller region above the North Pacific. The respective mean ERs are 1.78 ± 0.28 above northern Africa and the Middle East, 1.69 ± 0.26 above southern Africa, 1.62 ± 0.33 above South America, and 1.22 ± 0.22 in the latitude band 20–45° N. Probably due to its formation as a secondary product of biomass burning, there is hardly any information on emission factors of PAN in the literature. From the ERs given in Tereszchuk et al. (2013a) for ACE-FTS measurements in boreal fire plumes, we derived $\Delta PAN/\Delta HCN$ emission ratios covering the range of 0.9 to 2.75, most of them lying between 1 and 2.

In April, the region of high correlations has considerably expanded and nearly covers the whole latitude band from 10 to 40° N and the area between the tropical southern Atlantic, the southern Indian Ocean, and Australia. The respective ERs are 1.62 ± 0.28 (NHSUB), 1.27 ± 0.20 (SAM), 2.12 ± 0.77 (SAF), and 1.46 ± 0.32 (IOAUS), which is in the same range as in February. At northern middle and high latitudes, PAN is generally not correlated with HCN and the ERs are as high as 4 or more. Both findings indicate that the NH PAN increase in boreal spring rather has biogenic sources.

In July, the high correlations in the band 10 to 40° N are restricted to the region from the Middle East to the mid-Pacific. The mean ER above northern Africa and the Middle East, covering the western part of the AMA, is 1.93 ± 0.54, while it increases to 2.66 ± 0.91 in the region NHSUB. The band is interrupted by an area of low correlations, extending from the Gulf of Mexico above the tropical Atlantic to Europe. Low correlations were also observed over Europe, Siberia, northern Canada, and the Arctic. All these regions are characterized by very high ERs of more than 4. Both the low correlations and the high ERs hint at major contributions from anthropogenic or biogenic sources for the PAN enhancements, as outlined in the Appendix. As shown in Fig. 7, the northern extratropical PAN–HCN correlations in August and September are higher, which indicates PAN release from biomass burning during this time. Another region with high correlations in July is southern Africa and the adjacent southern Atlantic. The mean ER for this region, dominated by pollution from biomass burning, is 1.16 ± 0.17, which is lower than the northern hemispheric values.

Like for the other pollutants, there is a large region of high correlations in the Southern Hemisphere in October, extending from tropical South America over the southern Atlantic to southern Africa and continuing in a band at southern midlatitudes. High correlations were also observed in adjacent regions above northeastern Africa and the eastern Pacific. The correlations are comparably strong, like those for C_2H_2 versus HCN. The mean ERs are 1.09 ± 0.27 above South America, 1.00 ± 0.28 above southern Africa, and 0.61 ± 0.20 above Indonesia and Australia. Again, the low value in the region around Indonesia and Australia (IOAUS) might also be caused by contributions of peat fires. The somewhat higher

ERs above northern Africa and eastward of tropical South America point to additional or different pollution processes.

HCOOH versus HCN

In Fig. 13, we show correlation coefficients and enhancement ratios for HCOOH versus HCN. In February, there are only a few bins with mean HCOOH VMRs larger than 60 pptv. A contiguous area of high correlations is situated above northeastern Africa. The respective mean enhancement ratio for bins with $r > 0.6$ is 0.77 ± 0.28, which is clearly above the emission ratio for savanna burning (0.28) but close to the values for tropical forest fires (0.65) and for burning of agricultural residues (0.78). Like for $\Delta C_2H_6/\Delta HCN$, this implies either the observation of pollution by tropical forest fires or by burning of agricultural residues instead of savanna fires or biogenic contributions to the enhanced HCOOH. However, when discussing $\Delta HCOOH/\Delta HCN$ enhancement ratios, the same caveats with respect to plume aging have to be taken into account as for $\Delta C_2H_2/\Delta HCN$. The other regions around 45° N, South America and the southern tropical Atlantic, mostly exhibit moderately strong correlations only and a larger variation both in r and in the ERs, giving no clear picture.

In April, the area of high correlations above northeastern Africa somewhat increases. The mean ER in this region is 0.57 ± 0.15, which corresponds well with the emission ratios for tropical forest fires. However, compared to February, it can also be an indication for aged pollution. Similarly to the other pollutants, very high correlations were observed in the latitude band 20–40° N above the Pacific, the United States, and the North Atlantic. The mean ER in this area is 0.77 ± 0.27, which fits well to the emission ratios for tropical or temperate forest fires and for the burning of agricultural residues. There are only low to moderate correlations north of 40° N, indicating that the northern hemispheric HCOOH increase in spring (cf. Fig. 5) is not caused by biomass burning but rather by the oxidation of biogenic precursors.

During August, most of the bins in the northern hemispheric extratropics exhibit moderately strong to strong correlations with HCN, with a focus above Siberia and northern North America. The mean ER for bins with $r > 0.6$ is 1.05 ± 0.66 for North America and 1.26 ± 0.45 for Siberia, which is in good agreement with the emission ratio of 1.15 for boreal forest fires. Thus, both the high correlations and the ERs indicate the release of HCOOH by boreal fires, but regions with lower correlations and high ERs, especially above the northeastern United States, point to biogenic sources as well (cf. Appendix, Figs. A2 and A3). Strong correlations were also observed above southern hemispheric tropical Africa and in a band between 30 and 50° S, extending from the South Atlantic eastward as far as New Zealand. The mean ER above southern Africa is 0.92 ± 0.79. Restricted to southern tropical Africa, it is even lower, namely 0.47 ± 0.08, which is in good agreement with the emission
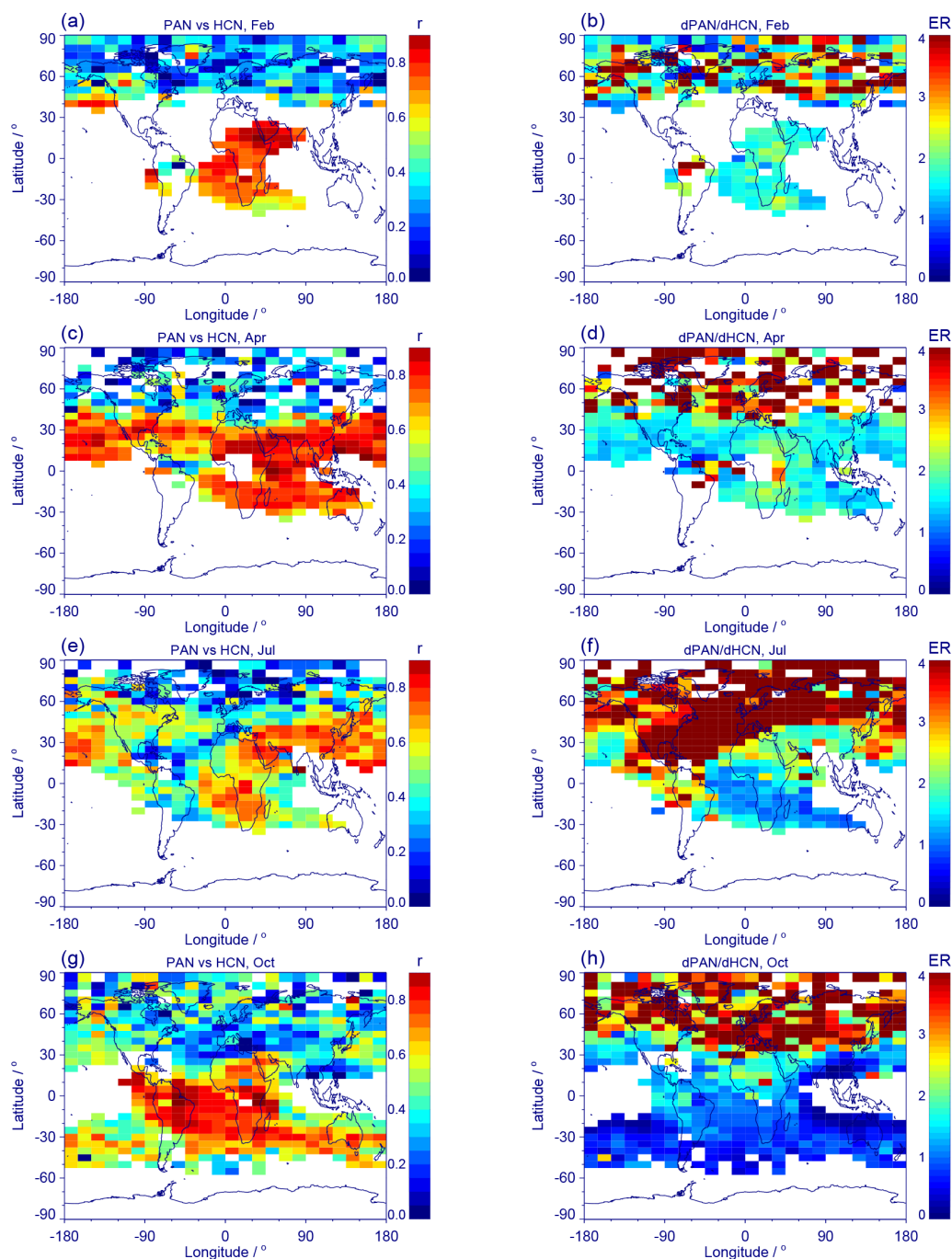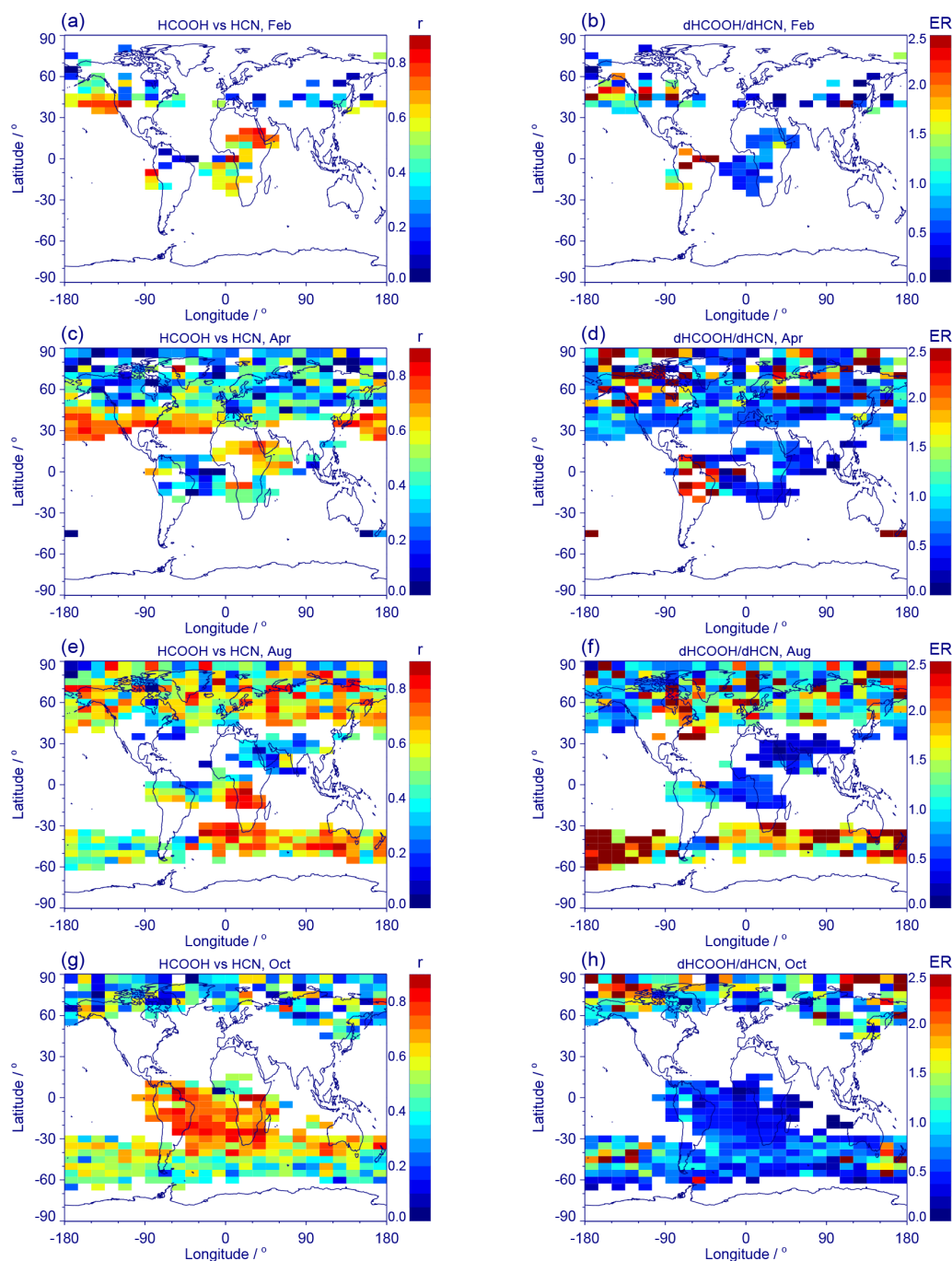
Figure 12. Global distribution of correlation coefficients r between MIPAS measurements of PAN and HCN in the upper troposphere for **(a)** February, **(c)** April, **(e)** July, and **(g)** October, as well as the respective ΔPAN / ΔHCN enhancement ratios (ERs) in pptv pptv^{-1} for **(b)** February, **(d)** April, **(f)** July, and **(h)** October. White areas are regions with correlation coefficients or enhancement ratios lower than zero, with PAN VMRs lower than 100 pptv, or with bins containing fewer than 10 values. For further details, see Fig. 9.

ratio for tropical forest fires and savanna burning. In comparison, the correlation above South America is lower and the mean ER is 1.19 ± 0.26, which is clearly above the emission ratios for biomass burning, indicating biogenic release (cf. Fig. A3). The ERs in the southern hemispheric band at 40° S

are much higher, namely around 1.5 above the southern Atlantic and up to 2.5 or larger south of Australia and above the southern Pacific. Despite the high correlations with HCN south of Africa and south of Australia, the high ERs rather indicate a strong portion of biogenic sources of the enhanced

Figure 13. Global distribution of correlation coefficients r between MIPAS measurements of HCOOH and HCN in the upper troposphere for **(a)** February, **(c)** April, **(e)** August, and **(g)** October, as well as the respective ΔHCOOH/ΔHCN enhancement ratios (ERs) in pptv pptv^{-1} for **(b)** February, **(d)** April, **(f)** August, and **(h)** October. White areas are regions with correlation coefficients lower than zero, with HCOOH VMRs lower than 60 pptv, or with bins containing fewer than 10 values. For further details see Fig. 9.

HCOOH in this latitude band during this time of the year. As shown in Fig. A3, a clear region of biogenic sources is tropical South America, but sources in central/western Africa can contribute as well.

In October, there are strong correlations in the area between South America and southern Africa and somewhat lower ones in the region extending eastward to Australia. The mean ERs above South America and southern Africa are 0.54 ± 0.18 and 0.40 ± 0.11, respectively. The first value

is in good agreement with the emission ratio for tropical forest fires, and the second is in between the latter and the value for savanna burning. The high correlations indicate that biomass burning is a major source of the enhanced HCOOH observed in the southern tropics and subtropics during this period. However, contrary to the other short-lived pollutant C_2H_2, the October ERs of HCOOH have not yet decreased considerably with respect to the emission ratios for savanna or tropical forest fires. Thus, if we assume that the low $\Delta C_2H_2/\Delta HCN$ ERs reflect plume aging, this is an indication for the additional contribution of biogenic release or secondary production to the observed HCOOH amounts, giving the false impression of exclusively fresh pollution by biomass burning only. The correlations in the southern midlatitude band are not as high and exhibit a larger variation. The ERs above the band segment covering the southern Atlantic and the southern Indian Ocean are nearly as low as in the southern tropics, leading to a mean ER of 0.73 ± 0.25. This indicates that, in October, the dominant source of the enhanced HCOOH in this region is also biomass burning. However, especially above the South Pacific, there are still bins with ERs between 1 and more than 2.5, which point to biogenic sources or secondary HCOOH formation as well.

5 Summary and conclusions

We compared the seasonal distributions of upper-tropospheric HCN, CO, C_2H_2, C_2H_6, PAN, and HCOOH measured by MIPAS between July 2002 and April 2012 to distinguish between different sources of upper-tropospheric pollution. While enhanced HCN is regarded as a nearly unambiguous tracer of biomass burning, the other pollutants have anthropogenic or biogenic sources as well.

At northern middle and high latitudes, maximum HCN, CO, PAN, and HCOOH amounts were measured during spring and/or summer, and minima were measured during winter. On the contrary, maximum northern extratropical C_2H_2 and C_2H_6 amounts were observed during winter and spring, and minimum values were observed during summer and fall. The reason is the minimum of their dominant reactant, the OH radical, and enhanced biofuel and fossil fuel burning during winter. In the tropics and subtropics, enhanced amounts of all pollutants were observed during each season, especially widespread in the Southern Hemisphere during austral spring. Due to its long lifetime, enhanced HCN was even measured at high southern latitudes during austral summer. Another characteristic feature observed is transatlantic transport of C_2H_6 and PAN in boreal summer. This transport pattern is not accompanied by enhanced HCN, which points to C_2H_6 release from fossil fuel production and transport around the Gulf of Mexico and subsequent formation of PAN. Simultaneous observation of enhanced HCOOH indicates biogenic sources in the eastern United States as well. Biogenic sources of HCOOH can also be identified in

the Amazon region and, with certain limitations, in tropical Africa. Further measurements are the accumulation of pollutants in the Asian monsoon anticyclone during boreal summer and enhanced C_2H_2 over southeastern Asia in boreal winter.

To quantify the assumptions on the sources of the other pollutants, we additionally performed correlation analyses with HCN in latitude–longitude bins covering the whole upper troposphere. These analyses mostly confirmed the conclusions obtained from comparison of the VMR distributions. For example, in the area of the southern hemispheric biomass burning plume, the other pollutants are very well correlated with HCN. Also, a high correlation of C_2H_2 and PAN with HCN in the tropics during all other seasons generally points to biomass burning as an important source of these pollutants, while the weaker correlation of CO, C_2H_6, and HCOOH with HCN hints at additional anthropogenic and biogenic sources. The analysis also showed that the VMR enhancements of CO, PAN, and HCOOH in large regions north of $50°$ during boreal spring and early summer are rather uncorrelated or only moderately well correlated with HCN, indicating other anthropogenic and biogenic sources. In August and September, during and after the peak of the boreal fire season, the respective correlations become stronger, pointing to the release of these species by boreal fires as well.

Although the $\Delta HCN/\Delta CO$ enhancement ratios presented here are monthly composites, there is good agreement with ACE-FTS values derived from individual plumes in different global regions. Furthermore, the enhancement ratios determined for middle and high latitudes in July are in between the emission ratios derived from the emission factors for extratropical or boreal forest fires given in Andreae and Merlet (2001) and in Andreae (2019) but are a factor of 3–5 lower than the emission ratios corresponding to the values listed in Akagi et al. (2011). The $\Delta HCN/\Delta CO$ ERs obtained for the plume above northern tropical Africa and the Middle East during boreal spring are clearly below the respective emission ratios for biomass burning, indicating additional sources of the observed CO. In the southern hemispheric plume, the observed ERs agree well with the emission ratios for tropical forest fires and savanna burning derived from the emission factors given in Andreae (2019). They also match the values given in Akagi et al. (2011) but are significantly higher than the emission ratios corresponding to the values for savanna burning and for tropical forest fires of Andreae and Merlet (2001). The highest $\Delta HCN/\Delta CO$ enhancement ratios, observed above the tropical Indian Ocean and northern Australia, are most probably caused by intensive peat fires in Indonesia during the El Niño years 2002/03 and 2006/07.

Although C_2H_2 and HCOOH have a considerably shorter atmospheric lifetime than HCN, their enhancement ratios to HCN obtained for northern midlatitudes and high latitudes during August agree well with the emission ratios for boreal fires. The $\Delta C_2H_2/\Delta HCN$ ERs obtained for the pollution above northeastern Africa and the Middle East in boreal

spring fit well to the emission ratio for the major local burning process, namely savanna fires, but also to those for the burning of tropical forest and agricultural residuals. The respective $\Delta HCOOH/\Delta HCN$ ERs are clearly higher than the emission ratio for savanna fires and indicate tropical forest fires, the burning of agricultural residuals, or (considering the dominance attributed to savanna burning) the additional biogenic release of HCOOH. The $\Delta C_2H_6/\Delta HCN$ ERs at northern middle and high latitudes are higher than the emission ratios, indicating additional sources of C_2H_6. The respective ERs obtained for pollution above northeastern Africa also hint to tropical forest fires rather than savanna burning or alternatively to additional anthropogenic sources. For southern hemispheric biomass burning, the $\Delta C_2H_2/\Delta HCN$ ERs agree well with the emission ratios for savanna and tropical forest burning during August, while the October ERs indicate aged pollution. The SH $\Delta C_2H_6/\Delta HCN$ ERs are in good agreement with the emission ratios for savanna fires in both August and October. Especially above the Amazon region, the $\Delta HCOOH/\Delta HCN$ ERs for August are considerably higher than the emission ratios for savanna or tropical forest fires, indicating the biogenic release of HCOOH. In October, they fit better to these fire types, which hints to a large impact of biomass burning on enhanced southern hemispheric HCOOH during this time of the year.

Appendix A: Global distributions at 10–11 km altitude and at 5 km below the tropopause

Here we present regions of upper-tropospheric pollution, which become more visible at the geometrical altitude of 10 km and at 5 km below the tropopause.

Southern Asian biofuel burning

Especially in boreal winter, enhanced C_2H_2 VMRs, accompanied by low HCN amounts, were observed above southern and southeastern Asia around the altitude of 10 km (Fig. A1). At this height, one C_2H_2 plume is situated above central and northeastern Africa, and another one is situated above southern and southeastern Asia (Fig. A1a). Eastward outflow from the Asian plume leads to enhanced C_2H_2 above the subtropical northern Pacific, Central America, the United States, and even the northern Atlantic. There is also enhanced HCN over Africa but only background HCN over southeastern Asia and rather depleted HCN above the subtropical Pacific and Central America (Fig. A1b). This indicates that the source of the southeastern Asian C_2H_2 plume is not biomass burning but rather biofuel or fossil fuel combustion. Indeed, according to Streets et al. (2003), biofuel burning is the dominant source of C_2H_2 released in southern and southeastern Asia.

### Transatlantic transport in boreal summer

Figure A2 shows the global distribution of C_2H_6 and of other pollutants at 10 km altitude for the July composite. Air masses containing enhanced C_2H_6 amounts of up to 900 pptv, apparently originating from the Gulf of Mexico and the southeastern United States, are transported over the northern Atlantic towards Europe (Fig. A2a). Another region of enhanced C_2H_6 is the Pacific southwest of Central America. Transport of pollution into the upper troposphere above Central America is favored by strong convection during summer. The southern US is characterized by very strong convection during the North American monsoon as well (Randel et al., 2012, and references therein). The C_2H_6 plume extending from the Gulf region towards Europe is not correlated with C_2H_2 or HCN (Fig. A2b and c). This indicates that the enhanced C_2H_6 originates from losses during production and transport of oil and gas, e.g., by improperly operated gas flaring, in the Gulf region. According to Elvidge et al. (2016), the worldwide largest number of flare sites is located in the United States, with a focus near the Gulf of Mexico. A considerable number of further flare sites are in Mexico and in northern South America. Another source is the considerably increased fracking in the United States during the late MIPAS measurement period (Franco et al., 2016; Helmig et al., 2016). There is also no correlation with HCN and just a weak correlation with C_2H_2 above the Pacific southwest of Central America.

The spatially well correlated plume of enhanced PAN extending from the Gulf of Mexico towards Europe (Fig. A2d) hints at the generation of PAN as a secondary product of the hydrocarbons released by the oil and gas industries. However, the nearly congruent plume of HCOOH (Fig. A2e) points to strong biogenic activity as well and thus to the possible release of PAN precursors from biogenic sources. A correlation analysis for the pollutants in the plume extending above the northern Atlantic (30–45° N, 30–90° W) for the month of August results in Pearson correlation coefficients of $r = 0.50$ for HCOOH versus C_2H_6, of $r = 0.69$ for PAN versus C_2H_6, and of $r = 0.65$ for PAN versus HCOOH. This indicates a comparably weak interrelation between HCOOH and C_2H_6 but possible industrial and biogenic sources of the observed PAN. Biogenic release of the PAN precursor, acetone, from the southeastern United States was observed by Franco et al. (2019) in an analysis of data from the Infrared Atmospheric Sounding Interferometer (IASI) on the MetOp-A satellite. Measurements of the Ozone Monitoring Instrument (OMI) (http://www.temis.nl/airpollution, last access: 20 January 2025) show that a possible source of the NO_x amounts required for PAN formation is anthropogenic pollution in the eastern United States. However, lightning activity can also play a major role. According to Hudman et al. (2007), lightning is the dominant source of the upper-tropospheric NO_x observed during summer above the southeastern United States. Compared to the large plume above the
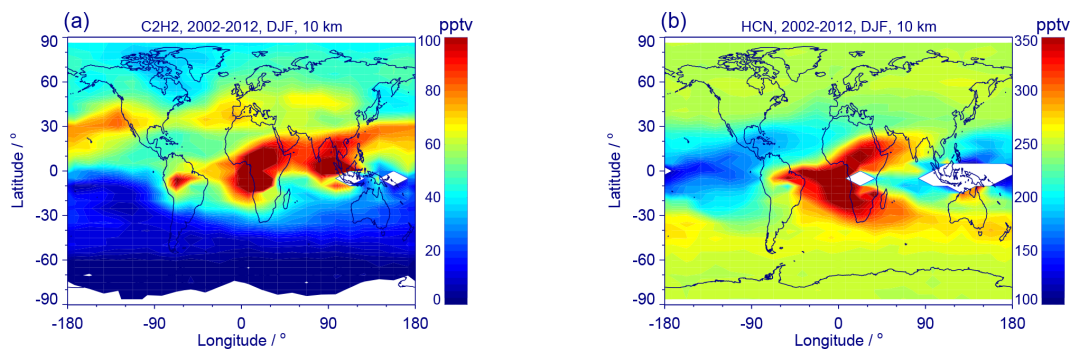
Figure A1. Global distributions of **(a)** C_2H_2 and **(b)** HCN measured by MIPAS at 10 km altitude during December to February, averaged over the time period 2002 to 2012. White areas: no data due to cloud filter.
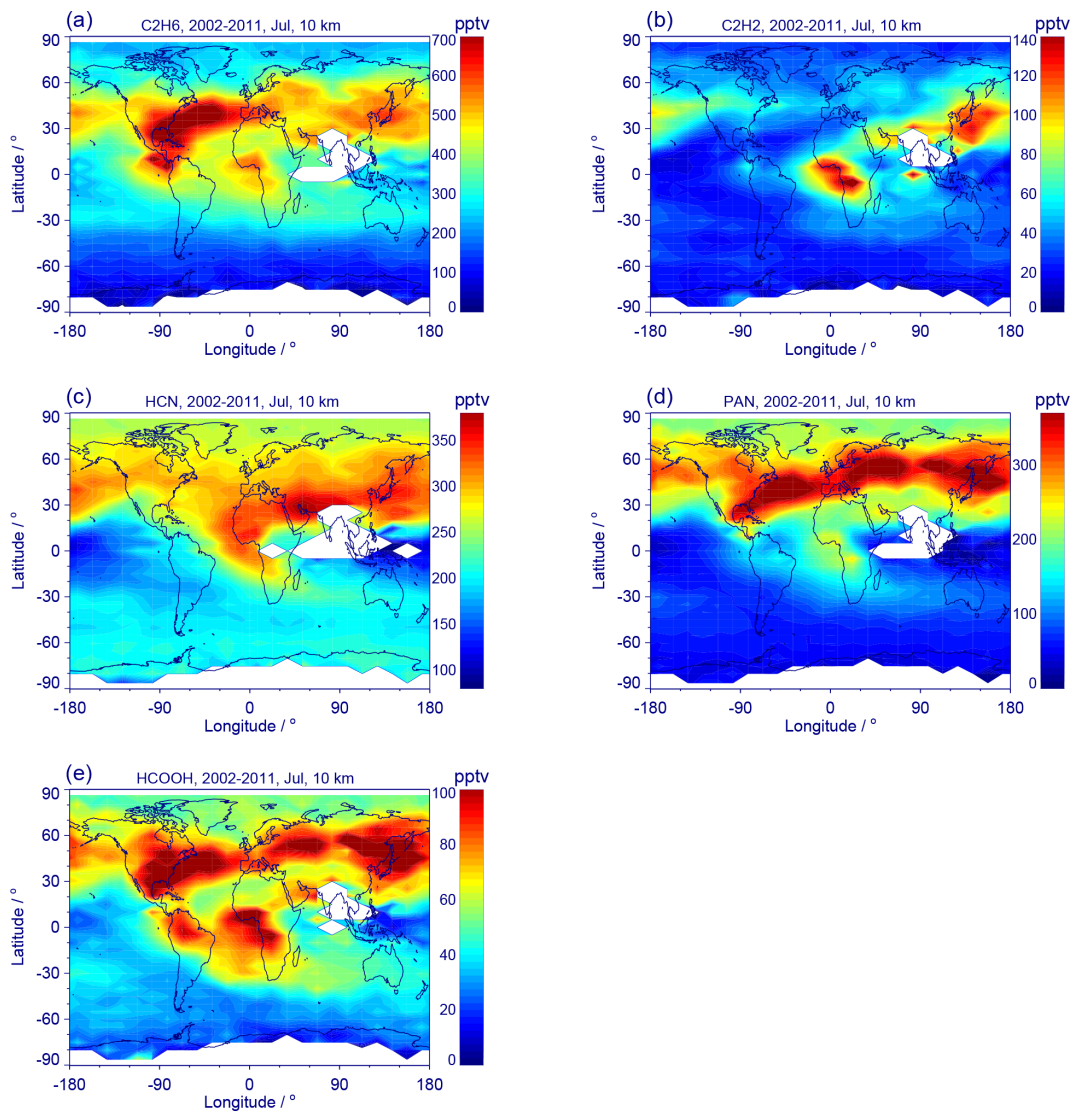
Figure A2. Global distributions of **(a)** C_2H_6, **(b)** C_2H_2, **(c)** HCN, **(d)** PAN, and **(e)** HCOOH measured by MIPAS at 10 km altitude during July, averaged over the time period 2002 to 2012.
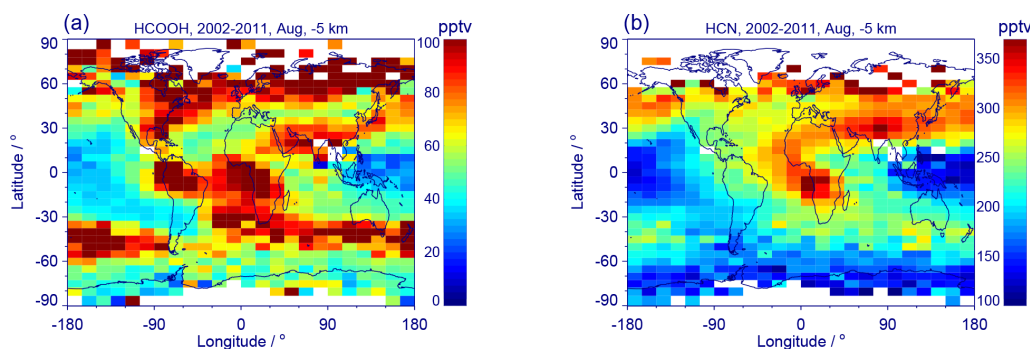
Figure A3. Global distributions of **(a)** HCOOH and **(b)** HCN measured by MIPAS at 5 km below the tropopause during August, averaged over the time period 2002 to 2012.

northern Atlantic, there is only a weak and spatially very restricted PAN enhancement over Central America. This might be due to lower amounts of NO_x in this region, as indicated by OMI measurements.

Global HCOOH and HCN during August

In Fig. A3, we show global distributions of the August composites of HCOOH and of HCN at 5 km below the tropopause. The HCOOH distribution (Fig. A3a) exhibits one tropical source in the Amazon region and another one in western/central Africa. The enhanced HCOOH amounts above tropical South America obviously originate from biogenic sources, since only background HCN amounts were observed there (Fig. A3b). The elevated HCOOH above western Africa is accompanied by a local HCN maximum, which, however, is centered somewhat further south. This hints to biogenic sources of the HCOOH observed in this region but to release by biomass burning as well. While the HCOOH enhancement at southern hemispheric midlatitudes is as strong as in the tropical source regions, HCN is only moderately enhanced in this region. This indicates that the HCOOH amounts observed at southern midlatitudes during August are also dominated by biogenic sources in tropical South America and potentially in western Africa as well.

As already shown in Fig. A2, there is another source of enhanced HCOOH in central and eastern North America with outflow over the northern Atlantic. Since these HCOOH enhancements are not correlated with HCN, they seem to also have biogenic sources. For the HCOOH enhancements above northern Europe, Siberia, and the Canadian Arctic, such a clear separation between biogenic sources and biomass burning can not be performed.

Spectroradiometer on the Terra satellite launched by NASA on 18 December 1999.

References

Akagi, S. K., Yokelson, R. J., Wiedinmyer, C., Alvarado, M. J., Reid, J. S., Karl, T., Crounse, J. D., and Wennberg, P. O.: Emission factors for open and domestic biomass burning for use in atmospheric models, Atmos. Chem. Phys., 11, 4039–4072, https://doi.org/10.5194/acp-11-4039-2011, 2011.

Andreae, M. O.: Emission of trace gases and aerosols from biomass burning – an updated assessment, Atmos. Chem. Phys., 19, 8523–8546, https://doi.org/10.5194/acp-19-8523-2019, 2019.

Andreae, M. O. and Merlet, P.: Emission of trace gases and aerosols from biomass burning, Global Biogeochem. Cy., 15, 955–966, https://doi.org/10.1029/2000GB001382, 2001.

Bernath, P. F., McElroy, C. T., Abrams, M. C., Boone, C. D., Butler, M., Camy-Peyret, C., Carleer, M., Clerbaux, C., Coheur, P.-F., Colin, R., DeCola, P., De Mazière, M., Drummond, J. R., Dufour, D., Evans, W. F. J., Fast, H., Fussen, D., Gilbert, K., Jennings, D. E., Llewellyn, E. J., Lowe, R. P., Mahieu, E., McConnell, J. C., McHugh, M., McLeod, S. D., Michaud, R., Midwinter, C., Nassar, R., Nichitiu, F., Nowlan, C., Rinsland, C. P., Rochon, Y. J., Rowlands, N., Semeniuk, K., Simon, P., Skelton, R., Sloan, J. J., Soucy, M.-A., Strong, K., Tremblay, P., Turnbull, D., Walker, K. A., Walkty, I., Wardle, D. A., Wehrle, V., Zander, R., and Zou, J.: Atmospheric Chemistry Experiment (ACE): Mission overview, Geophys. Res. Lett., 32, L15S01, https://doi.org/10.1029/2005GL022386, 2005.

Bertschi, I. T., Yokelson, R. J., Ward, D. E., Christian, T. J., and Hao, W. M.: Trace gas emissions from the production and use of domestic biofuels in Zambia measured by open-path Fourier transform infrared spectroscopy, J. Geophys. Res., 108, D8469, https://doi.org/10.1029/2002JD002158, 2003.

Blake, N. J., Blake, D. R., Sive, B. C., Chen, S. R., Collins, J. E. Jr., Sachse, G. W., and Anderson, B. E.: Biomass burning emissions and vertical distribution of atmospheric methyl halides and other reduced carbon gases in the South Atlantic region, J. Geophys. Res., 101, 24151–24164, https://doi.org/10.1029/96JD00561, 1996.

Blumstein, D., Chalon, G., Carlier, T., Buila, C., Hébert, P., Maciaszek, T., Ponce, G., Phulpin, T., Tournier, B., Siméoni, D., Astruc, P., Clauss, A., Kayal, G., and Jegou, R.: IASI instrument: Technical overview and measured performances, Proc. SPIE 5543, Infrared Spaceborne Remote Sensing XII, 4 November 2004, Denver, Colorado, https://doi.org/10.1117/12.560907, 2004.

Boone, C. D., Nassar, R., Walker, K. A., Rochon, Y., McLeod, S. D., Rinsland, C. P., and Bernath, P. F.: Retrievals for the atmospheric chemistry experiment Fourier-transform spectrometer, Appl. Optics, 44, 7218–7231, https://doi.org/10.1364/AO.44.007218, 2005.

Chen, Y., Hall, J., van Wees, D., Andela, N., Hantson, S., Giglio, L., van der Werf, G. R., Morton, D. C., and Randerson, J. T.: Multi-decadal trends and variability in burned area from the fifth version of the Global Fire Emissions Database (GFED5), Earth Syst. Sci. Data, 15, 5227–5259, https://doi.org/10.5194/essd-15-5227-2023, 2023.

Clerbaux, C., Boynard, A., Clarisse, L., George, M., Hadji-Lazaro, J., Herbin, H., Hurtmans, D., Pommier, M., Razavi, A., Turquety, S., Wespes, C., and Coheur, P.-F.: Monitoring of atmospheric composition using the thermal infrared IASI/MetOp sounder, Atmos. Chem. Phys., 9, 6041–6054, https://doi.org/10.5194/acp-9-6041-2009, 2009.

Court, A.: Tropopause Disappearance During the Antarctic Winter, B. Am. Meteorol. Soc., 23, 220–238, 1942.

Deming, W. E.: Statistical adjustment of data, Wiley, NY, Dover Publications edition, ISBN 0-486-64685-8, 1985.

Duflot, V., Wespes, C., Clarisse, L., Hurtmans, D., Ngadi, Y., Jones, N., Paton-Walsh, C., Hadji-Lazaro, J., Vigouroux, C., De Mazière, M., Metzger, J.-M., Mahieu, E., Servais, C., Hase, F., Schneider, M., Clerbaux, C., and Coheur, P.-F.: Acetylene (C_2H_2) and hydrogen cyanide (HCN) from IASI satellite observations: global distributions, validation, and comparison with model, Atmos. Chem. Phys., 15, 10509–10527, https://doi.org/10.5194/acp-15-10509-2015, 2015.

Duncan, B. N., Strahan, S. E., Yoshida, Y., Steenrod, S. D., and Livesey, N.: Model study of the cross-tropopause transport of biomass burning pollution, Atmos. Chem. Phys., 7, 3713–3736, https://doi.org/10.5194/acp-7-3713-2007, 2007.

Edwards, D. P., Emmons, L. K., Gille, J. C., Chu, A., Attié, J.-L., Giglio, L., Wood, S. W., Haywood, J., Deeter, M. N., Massie, S. T., Ziskin, D. C., and Drummond, J. R.: Satellite–observed pollution from Southern Hemisphere biomass burning, J. Geophys. Res., 111, D14312, https://doi.org/10.1029/2005JD006655, 2006.

Elvidge, C. D., Zhizhin, M., Baugh, K., Hsu, F.-C., and Ghosh, T.: Methods for Global Survey of Natural Gas Flaring from Visible Infrared Imaging Radiometer Suite Data, Energies, 9, 14, https://doi.org/10.3390/en9010014, 2016.

European Space Agency: Envisat, MIPAS An instrument for atmospheric chemistry and climate research, ESA Publications Division, ESTEC, P.O. Box 299, 2200 AG Noordwijk, the Netherlands, SP-1229, https://doi.org/10.1117/12.560907, 2000.

Fischer, E. V., Jacob, D. J., Yantosca, R. M., Sulprizio, M. P., Millet, D. B., Mao, J., Paulot, F., Singh, H. B., Roiger, A., Ries, L., Talbot, R. W., Dzepina, K., and Pandey Deolal, S.: Atmospheric peroxyacetyl nitrate (PAN): a global budget and source attribution, Atmos. Chem. Phys., 14, 2679–2698, https://doi.org/10.5194/acp-14-2679-2014, 2014.

Fischer, H., Birk, M., Blom, C., Carli, B., Carlotti, M., von Clarmann, T., Delbouille, L., Dudhia, A., Ehhalt, D., Endemann, M.,

Flaud, J. M., Gessner, R., Kleinert, A., Koopman, R., Langen, J., López-Puertas, M., Mosner, P., Nett, H., Oelhaf, H., Perron, G., Remedios, J., Ridolfi, M., Stiller, G., and Zander, R.: MIPAS: an instrument for atmospheric and climate research, Atmos. Chem. Phys., 8, 2151–2188, https://doi.org/10.5194/acp-8-2151-2008, 2008.

Franco, B., Mahieu, E., Emmons, L. K., Tzompa-Sosa, Z. A., Fischer, E. V., Sudo, K., Bovy, B., Conway, S., Griffin, D., Hannigan, J. W., Strong, K., and Walker, K. A.: Evaluating ethane and methane emissions associated with the development of oil and natural gas extraction in North America, Environ. Res. Lett., 11, 044010, https://doi.org/10.1088/1748-9326/11/4/044010, 2016.

Franco, B., Clarisse, L., Stavrakou, T., Müller, J.-F., Pozzer, A., Hadji-Lazaro, J., Hurtmans, D., Clerbaux, C., and Coheur, P.-F.: Acetone Atmospheric Distribution Retrieved From Space, Geophys. Res. Lett., 46, 2884–2893, https://doi.org/10.1029/2019GL082052, 2019.

Franco, B., Clarisse, L., Stavrakou, T., Müller, J.-F., Taraborrelli, D., Hadji-Lazaro, J., Hannigan, J. W., Hase, F., Hurtmans, D., Jones, N., Lutsch, E., Mahieu, E., Ortega, I., Schneider, M., Strong, K., Vigouroux, C., Clerbaux, C., and Coheur, P.-F.: Spaceborne Measurements of Formic and Acetic Acids: A Global View of the Regional Sources, Geophys. Res. Lett., 47, e2019GL086239, https://doi.org/10.1029/2019GL086239, 2020.

Funke, B., López-Puertas, M., García-Comas, M., Stiller, G. P., von Clarmann, T., Höpfner, M., Glatthor, N., Grabowski, U., Kellmann, S., and Linden, A.: Carbon monoxide distributions from the upper troposphere to the mesosphere inferred from 4.7 μm non-local thermal equilibrium emissions measured by MIPAS on Envisat, Atmos. Chem. Phys., 9, 2387–2411, https://doi.org/10.5194/acp-9-2387-2009, 2009.

Gaffney, J. S., Marley, N. A., Cunningham, M. M., and Doskey, P. V.: Measurements of peroxyacyl nitrates (PANS) in Mexico City: implications for megacity air quality impacts on regional scales, Atmos. Environ., 33, 5003–5012, 1999.

George, M., Clerbaux, C., Bouarar, I., Coheur, P.-F., Deeter, M. N., Edwards, D. P., Francis, G., Gille, J. C., Hadji-Lazaro, J., Hurtmans, D., Inness, A., Mao, D., and Worden, H. M.: An examination of the long-term CO records from MOPITT and IASI: comparison of retrieval methodology, Atmos. Meas. Tech., 8, 4313–4328, https://doi.org/10.5194/amt-8-4313-2015, 2015.

Glatthor, N., von Clarmann, T., Fischer, H., Funke, B., Grabowski, U., Höpfner, M., Kellmann, S., Kiefer, M., Linden, A., Milz, M., Steck, T., and Stiller, G. P.: Global peroxyacetyl nitrate (PAN) retrieval in the upper troposphere from limb emission spectra of the Michelson Interferometer for Passive Atmospheric Sounding (MIPAS), Atmos. Chem. Phys., 7, 2775–2787, https://doi.org/10.5194/acp-7-2775-2007, 2007.

Glatthor, N., von Clarmann, T., Stiller, G. P., Funke, B., Koukouli, M. E., Fischer, H., Grabowski, U., Höpfner, M., Kellmann, S., and Linden, A.: Large-scale upper tropospheric pollution observed by MIPAS HCN and C_2H_6 global distributions, Atmos. Chem. Phys., 9, 9619–9634, https://doi.org/10.5194/acp-9-9619-2009, 2009.

Glatthor, N., Höpfner, M., Stiller, G. P., von Clarmann, T., Funke, B., Lossow, S., Eckert, E., Grabowski, U., Kellmann, S., Linden, A., A. Walker, K., and Wiegele, A.: Seasonal and interannual variations in HCN amounts in the upper troposphere and lower stratosphere observed by MIPAS, Atmos. Chem. Phys., 15, 563–582, https://doi.org/10.5194/acp-15-563-2015, 2015.

Goldstein, A. H., Wofsy, S. C., and Spivakovsky, C. M.: Seasonal variations of nonmethane hydrocarbons in rural New England: Constraints on OH concentrations in northern midlatitudes, J. Geophys. Res., 100, 21023–21033, https://doi.org/10.1029/95JD02034, 1995.

González Abad, G., Bernath, P. F., Boone, C. D., McLeod, S. D., Manney, G. L., and Toon, G. C.: Global distribution of upper tropospheric formic acid from the ACE-FTS, Atmos. Chem. Phys., 9, 8039–8047, https://doi.org/10.5194/acp-9-8039-2009, 2009.

González Abad, G., Allen, N. D. C., Bernath, P. F., Boone, C. D., McLeod, S. D., Manney, G. L., Toon, G. C., Carouge, C., Wang, Y., Wu, S., Barkley, M. P., Palmer, P. I., Xiao, Y., and Fu, T. M.: Ethane, ethyne and carbon monoxide concentrations in the upper troposphere and lower stratosphere from ACE and GEOS-Chem: a comparison study, Atmos. Chem. Phys., 11, 9927–9941, https://doi.org/10.5194/acp-11-9927-2011, 2011.

Grutter, M., Glatthor, N., Stiller, G. P., Fischer, H., Grabowski, U., Höpfner, M., Kellmann, S., Linden, A., and von Clarmann, T.: Global distribution and variability of formic acid as observed by MIPAS-ENVISAT, J. Geophys. Res., 115, D10303, https://doi.org/10.1029/2009JD012980, 2010.

Guenther, A., Karl, T., Harley, P., Wiedinmyer, C., Palmer, P. I., and Geron, C.: Estimates of global terrestrial isoprene emissions using MEGAN (Model of Emissions of Gases and Aerosols from Nature), Atmos. Chem. Phys., 6, 3181–3210, https://doi.org/10.5194/acp-6-3181-2006, 2006.

Helmig, D., Munóz, M., Hueber, J., Mazzoleni, C., Mazzoleni, L., Owen, R. C., Val-Martin, M., Fialho, P., Plass-Duelmer, C., Palmer, P. I., Lewis, A. C., and Pfister, G.: Climatology and atmospheric chemistry of the nonmethane hydrocarbons ethane and propane over the North Atlantic, Elementa: Science of the Anthropocene, 3, 000054, https://doi.org/10.12952/journal.elementa.000054, 2015.

Helmig, D., Rossabi, S., Hueber, J., Tans, P., Montzka, S. A., Masarie, K., Thoning, K., Plass-Duelmer, C., Claude, A., Carpenter, L. J., Lewis, A. C., Punjabi, S., Reimann, S., Vollmer, M. K., Steinbrecher, R., Hannigan, J. W., Emmons, L. K., Mahieu, E., Franco, B., Smale, D., and Pozzer, A.: Reversal of global atmospheric ethane and propane trends largely due to US oil and natural gas production, Nat. Geosci., 9, 490–495, https://doi.org/10.1038/ngeo2721, 2016.

Hilton, F., Armante, R., August, T., Barnet, C., Bouchard, A., Camy-Peyret, C., Capelle, V., Clarisse, L., Clerbaux, C., Coheur, P.-F., Collard, A., Crevoisier, C., Dufour, G., Edwards, D., Faijan, F., Fourrié, N., Gambacorta, A., Goldberg, M., Guidard, V., Hurtmans, D., Illingworth, S., Jacquinet-Husson, N., Kerzenmacher, T., Klaes, D., Lavanant, L., Masiello, G., Matricardi, M., McNally, A., Newman, S., Pavelin, E., Payan, S., Péquinot, E., Peyridieu, S., Phulpin, T., Remedios, J., Schlüssel, P., Serio, C., Strow, L., Stubenrauch, C., Taylor, J., Tobin, D., Wolf, W., and Zhou, D.: Hyperspectral earth observation with IASI, B. Am. Meteorol. Soc., 93, 347–370, https://doi.org/10.1175/BAMS-D-11-00027.1, 2012.

Hobbs, P. V., Sinha, P., Yokelson, R. J., Christian, T. J., Blake, D. R., Gao, S., Kirchstetter, T. W., Novakov, T., and Pilewskie, P.: Evolution of gases and particles from a sa-

vanna fire in South Africa, J. Geophys. Res., 108, 8485, https://doi.org/10.1029/2002JD002352, 2003.

Höpfner, M., von Clarmann, T., Fischer, H., Glatthor, N., Grabowski, U., Kellmann, S., Kiefer, M., Linden, A., Mengistu Tsidu, G., Milz, M., Steck, T., Stiller, G. P., Wang, D.-Y., and Funke, B.: First spaceborne observations of Antarctic stratospheric $ClONO_2$ recovery: Austral spring 2002, J. Geophys. Res., 109, D11308, https://doi.org/10.1029/2004JD004609, 2004.

Hough, A. M.: Development of a Two-Dimensional Global Tropospheric Model: Model Chemistry, J. Geophys. Res., 96, 7325–7362, 1991.

Hudman, R. C., Jacob, D. J., Turquety, S., Leibensperger, E. M., Murray, L. T., Wu, S., Gilliland, A. B., Avery, M., Bertram, T. H., Brune, W., Cohen, R. C., Dibb, J. E., Flocke, F. M., Fried, A., Holloway, J., Neuman, J. A., Orville, R., Perring, A., Ren, X., Sachse, G. W., Singh, H. B., Swanson, A., and Wooldridge, P. J.: Surface and lightning sources of nitrogen oxides over the United States: Magnitudes, chemical evolution, and outflow, J. Geophys. Res., 112, D12S05, https://doi.org/10.1029/2006JD007912, 2007.

Justice, C. O., Giglio, L., Korontzi, S., Owens, J., Morisette, J. T., Roy, D., Descloitres, J., Alleaume, S., Petitcolin, F., and Kaufman, Y.: The MODIS fire products, Remote Sens. Environ., 83, 244–262, https://doi.org/10.1016/S0034-4257(02)00076-7, 2002.

Keene, W. C. and Galloway, J. N.: The biogeochemical cycling of formic and acetic acids through the troposphere: an overview of current understanding, Tellus B, 40, 322–334, 1988.

KIT (Karlsruhe Institute of Technology): Access to IMK/IAA generated MIPAS/Envisat data, KIT [data set], https://www.imk-asf.kit.edu/english/308.php (last access: 21 January 2025), 2024.

Lefer, B. L., Talbot R. W., Harriss, R. H., Bradshaw, J. D., Sandholm, S. T., Olson, J. O., Sachse, G. W., Collins, J., Shipham, M. A., Blake, D. R., Klemm, K. I., Klemm, O., Gorzelska, K., and Barrick, J.: Enhancement of acidic gases in biomass burning impacted air masses over Canada, J. Geophys. Res., 99, 1721–1737, https://doi.org/10.1029/93JD02091, 1994.

Lewis, S. L., Brando, P. M., Phillips, O. L., van der Heijden, G. M. F., and Nepstad, D.: The 2010 Amazon drought, Science, 331, 554–554, https://doi.org/10.1126/science.1200807, 2011.

Li, Q., Jacob, D. J., Bey, I., Yantosca, R. M., Zhao, Y., Kondo, Y., and Notholt, J.: Atmospheric hydrogen cyanide (HCN): biomass burning source, ocean sink?, Geophys. Res. Lett., 27, 357–360, 2000.

Li, Q., Jacob, D. J., Yantosca, R. M., Heald, C. L., Singh, H. B., Koike, M., Zhao. Y., Sachse, G. W., and Streets, D. G.: A global three-dimensional model analysis of the atmospheric budgets of HCN and CH_3CN: constraints from aircraft and ground measurements, J. Geophys. Res., 108, 8827, https://doi.org/10.1029/2002JD003075, 2003.

Lupu, A., Kaminski, J. W., Neary, L., McConnell, J. C., Toyota, K., Rinsland, C. P., Bernath, P. F., Walker, K. A., Boone, C. D., Nagahama, Y., and Suzuki, K.: Hydrogen cyanide in the upper troposphere: GEM-AQ simulation and comparison with ACE-FTS observations, Atmos. Chem. Phys., 9, 4301–4313, https://doi.org/10.5194/acp-9-4301-2009, 2009.

Mikkonen, S., Pitkänen, M. R. A., Nieminen, T., Lipponen, A., Isokääntä, S., Arola, A., and Lehtinen, K. E. J.: Technical note: Effects of uncertainties and number of data points on line fitting – a case study on new particle formation, Atmos. Chem. Phys., 19, 12531–12543, https://doi.org/10.5194/acp-19-12531-2019, 2019.

Nett, H., Perron, G., Sanchez, M., Burgess, A., and Mossner, P.: MIPAS inflight calibration and processor validation, in: EN-VISAT Calibration Review – Proc. of the European Workshop, 9–13 September 2002, ESTEC, Noordwijk, the Netherlands, CD-ROM, vol. SP-520, edited by: Sawaya-Lacoste, H., ESA Publications Division, ESTEC, Postbus 299, 2200 AG Noordwijk, the Netherlands, ISBN 92-9092-830-1, 2002.

Park, M., Randel, W. J., Kinnison, D. E., Emmons, L. K., Bernath, P. F., Walker, K. A., Boone, C. D., and Livesey, N. J.: Hydrocarbons in the upper troposphere and lower stratosphere observed from ACE-FTS and comparisons with WACCM, J. Geophys. Res., 118, 1964–1980, https://doi.org/10.1029/2012JD018327, 2013.

Pommier, M., Clerbaux, C., Coheur, P.-F., Mahieu, E., Müller, J.-F., Paton-Walsh, C., Stavrakou, T., and Vigouroux, C.: HCOOH distributions from IASI for 2008–2014: comparison with ground-based FTIR measurements and a global chemistry-transport model, Atmos. Chem. Phys., 16, 8963–8981, https://doi.org/10.5194/acp-16-8963-2016, 2016.

Randel, W. J., Moyer, E., Park, M., Jensen, E., Bernath, P., Walker, K., and Boone, C.: Global variations of HDO and HDO/H_2O ratios in the upper troposphere and lower stratosphere derived from ACE-FTS satellite measurements, J. Geophys. Res., 117, D06303, https://doi.org/10.1029/2011JD016632, 2012.

Reichler, T., Dameris, M., and Sausen, R.: Determining the tropopause height from gridded data, Geophys. Res. Lett., 30, 2042, https://doi.org/10.1029/2003GL018240, 2003.

Remedios, J. J., Leigh, R. J., Waterfall, A. M., Moore, D. P., Sembhi, H., Parkes, I., Greenhough, J., Chipperfield, M. P., and Hauglustaine, D.: MIPAS reference atmospheres and comparisons to V4.61/V4.62 MIPAS level 2 geophysical data sets, Atmos. Chem. Phys. Discuss., 7, 9973–10017, https://doi.org/10.5194/acpd-7-9973-2007, 2007.

Rinsland, C. P., Jones, N. B., Connor, B. J., Logan, J. A., Pougatchev, N. S., Goldman, A., Murcray, F. J., Stephen, T. M., Pine, A. S., Zander, R., Mahieu, E., and Demoulin, P.: Northern and southern hemisphere ground-based infrared spectroscopic measurements of tropospheric carbon monoxide and ethane, J. Geophys. Res., 103, 28197–28217, 1998.

Rudolph, J.: The tropospheric distribution and budget of ethane, J. Geophys. Res., 100, 11369–11381, 1995.

Rudolph, J., Ehhalt, D. H., and Khedim, A.: Vertical Profiles of Acetylene in the Troposphere and Stratosphere, J. Atmos. Chem., 2, 117–124, 1984.

Sanhueza, E., Santana, M., Trapp, D., deServes, C., Figueroa, L., Romero, R., Rondón, A., and Donoso, L.: Field measurement evidence for an atmospheric chemical source of formic and acetic acids in the tropic, Geophys. Res. Lett., 32, 1045–1048, 1996.

Singh, H., Chen, Y., Staudt, A., Jacob, D., Blake, D., Heikes, B., and Snow, J.: Evidence from the Pacific troposphere for large global sources of oxygenated organic compounds, Nature, 410, 1078–1081, https://doi.org/10.1038/35074067, 2001.

Singh, H. B.: Reactive nitrogen in the troposphere, Environ. Sci. Technol., 21, 320–327, 1987.

Singh, H. B., Herlth, D., Kolyer, R., Chatfield, R., Viezee, W., Salas, L. J., Chen, Y., Bradshaw, J. D., Sandholm, S. T., Talbot, R., Gregory, G. L., Anderson, B., Sachse, G. W., Browell, E., Bachmeier, A. S., Blake, D. R., Heikes, B., Jacob, D., and Fuelberg, H. E.: Impact of biomass burning emissions on the composition of the South Atlantic troposphere: Reactive nitrogen and ozone, J. Geophys. Res., 101, 24203–24219, 1996.

Singh, H. B., Salas, L., Herlth, D., Kolyer, R., Czech, E., Viezee, W., Li, Q., Jacob, D. J., Blake, D., Sachse, G., Harward, C. N., Fuelberg, H., Kiley, C. M., Zhao, Y., and Kondo, Y.: In situ measurements of HCN and CH_3CN over the Pacific Ocean: sources, sinks and budgets, J. Geophys. Res., 108, 8795, https://doi.org/10.1029/2002JD003006, 2003.

Stavrakou, T., Müller, J.-F., Peeters, J., Razavi, A., Clarisse, L., Clerbaux, C., Coheur, P.-F., Hurtmans, D., De Mazière, M., Vigouroux, C., Deutscher, N. M., Griffith, D. W. T., Jones, N., and Paton-Walsh, C.: Satellite evidence for a large source of formic acid from boreal and tropical forests, Nat. Geosci., 5, 26–30, 2012.

Steck, T.: Methods for determining regularization for atmospheric retrieval problems, Appl. Optics, 41, 1788–1797, 2002.

Stein, A. F., Draxler, R. R., Rolph, G. D., Stunder, B. J. B., and Cohen, M. D.: NOAA's HYSPLIT Atmospheric Transport and Dispersion Modeling System, B. Am. Meteorol. Soc., 96, 2059–2077, https://doi.org/10.1175/BAMS-D-14-00110.1, 2015.

Stiller, G. P. (Ed.): The Karlsruhe Optimized and Precise Radiative transfer Algorithm (KOPRA), Institut für Meteorologie und Klimaforschung, Forschungszentrum Karlsruhe GmbH, https://doi.org/10.5445/IR/270048971, 2000.

Streets, D. G. Bond, T. C., Carmichael, G. R., Fernandes, S. D., Fu, Q., He, D., Klimont, Z., Nelson, S. M., Tsai, N. Y., Wang, M. Q., Woo, J.-H., and Yarber, K. F.: An inventory of gaseous and primary aerosol emissions in Asia in the year 2000, J. Geophys. Res., 108, 8809, https://doi.org/10.1029/2002JD003093, 2003.

Tereszchuk, K. A., González Abad, G., Clerbaux, C., Hurtmans, D., Coheur, P.-F., and Bernath, P. F.: ACE-FTS measurements of trace species in the characterization of biomass burning plumes, Atmos. Chem. Phys., 11, 12169–12179, https://doi.org/10.5194/acp-11-12169-2011, 2011.

Tereszchuk, K. A., González Abad, G., Clerbaux, C., Hadji-Lazaro, J., Hurtmans, D., Coheur, P.-F., and Bernath, P. F.: ACE-FTS observations of pyrogenic trace species in boreal biomass burning plumes during BORTAS, Atmos. Chem. Phys., 13, 4529–4541, https://doi.org/10.5194/acp-13-4529-2013, 2013a.

Tereszchuk, K. A., Moore, D. P., Harrison, J. J., Boone, C. D., Park, M., Remedios, J. J., Randel, W. J., and Bernath, P. F.: Observations of peroxyacetyl nitrate (PAN) in the upper troposphere by the Atmospheric Chemistry Experiment-Fourier Transform Spectrometer (ACE-FTS), Atmos. Chem. Phys., 13, 5601–5613, https://doi.org/10.5194/acp-13-5601-2013, 2013b.

Tikhonov, A.: On the solution of incorrectly stated problems and a method of regularization, Dokl. Acad. Nauk SSSR+, 151, 501, 1963.

van der Werf, G. R., Randerson, J. T., Giglio, L., Collatz, G. J., Mu, M., Kasibhatla, P. S., Morton, D. C., DeFries, R. S., Jin, Y., and van Leeuwen, T. T.: Global fire emissions and the contribution of deforestation, savanna, forest, agricultural, and peat fires (1997–2009), Atmos. Chem. Phys., 10, 11707–11735, https://doi.org/10.5194/acp-10-11707-2010, 2010.

van der Werf, G. R., Randerson, J. T., Giglio, L., van Leeuwen, T. T., Chen, Y., Rogers, B. M., Mu, M., van Marle, M. J. E., Morton, D. C., Collatz, G. J., Yokelson, R. J., and Kasibhatla, P. S.: Global fire emissions estimates during 1997–2016, Earth Syst. Sci. Data, 9, 697–720, https://doi.org/10.5194/essd-9-697-2017, 2017.

van Wees, D., van der Werf, G. R., Randerson, J. T., Rogers, B. M., Chen, Y., Veraverbeke, S., Giglio, L., and Morton, D. C.: Global biomass burning fuel consumption and emissions at 500 m spatial resolution based on the Global Fire Emissions Database (GFED), Geosci. Model Dev., 15, 8411–8437, https://doi.org/10.5194/gmd-15-8411-2022, 2022.

Viatte, C., Strong, K., Hannigan, J., Nussbaumer, E., Emmons, L. K., Conway, S., Paton-Walsh, C., Hartley, J., Benmergui, J., and Lin, J.: Identifying fire plumes in the Arctic with tropospheric FTIR measurements and transport models, Atmos. Chem. Phys., 15, 2227–2246, https://doi.org/10.5194/acp-15-2227-2015, 2015.

Vogel, B., Günther, G., Müller, R., Grooß, J.-U., and Riese, M.: Impact of different Asian source regions on the composition of the Asian monsoon anticyclone and of the extratropical lowermost stratosphere, Atmos. Chem. Phys., 15, 13699–13716, https://doi.org/10.5194/acp-15-13699-2015, 2015.

von Clarmann, T., Fischer, H., Funke, B., Glatthor, N., Grabowski, U., Höpfner, M., Kellmann, S., Kiefer, M., Linden, A., Mengistu Tsidu, G., Milz, M., Steck, T., Stiller, G. P., Wang, D.-Y., Gil-López, S., and López-Puertas, M.: Retrieval of temperature and tangent altitude pointing from limb emission spectra recorded from space by the Michelson Interferometer for Passive Atmospheric Sounding (MIPAS), J. Geophys. Res., 108, D23, https://doi.org/10.1029/2003JD003602, 2003.

von Clarmann, T., Höpfner, M., Kellmann, S., Linden, A., Chauhan, S., Funke, B., Grabowski, U., Glatthor, N., Kiefer, M., Schieferdecker, T., Stiller, G. P., and Versick, S.: Retrieval of temperature, H_2O, O_3, HNO_3, CH_4, N_2O, $ClONO_2$ and ClO from MIPAS reduced resolution nominal mode limb emission measurements, Atmos. Meas. Tech., 2, 159–175, https://doi.org/10.5194/amt-2-159-2009, 2009.

Wiegele, A., Glatthor, N., Höpfner, M., Grabowski, U., Kellmann, S., Linden, A., Stiller, G., and von Clarmann, T.: Global distributions of C_2H_6, C_2H_2, HCN, and PAN retrieved from MIPAS reduced spectral resolution measurements, Atmos. Meas. Tech., 5, 723–734, https://doi.org/10.5194/amt-5-723-2012, 2012.

Xiao, Y., Jacob, D. J., and Turquety, S.: Atmospheric acetylene and its relationship with CO as an indicator of air mass age, J. Geophys. Res., 112, D12305, https://doi.org/10.1029/2006JD008268, 2007.

Xiao, Y., Logan, J. A., Jacob, D. J., Hudman, R. C., Yantosca, R., and Blake, D. R.: Global budget of ethane and regional constraints on US sources, J. Geophys. Res., 113, D21306, https://doi.org/10.1029/2007JD009415, 2008.

Yokelson, R. J., Bertschi, I. T., Christian, T. J., Hobbs, P. V., Ward, D. E., and Hao, W. M.: Trace gas measurements in nascent, aged, and cloud-processed smoke from African savanna fires by airborne Fourier transform infrared spectroscopy (AFTIR), J. Geophys. Res., 108, 8478, https://doi.org/10.1029/2002JD002322, 2003.

Yokelson, R. J., Urbanski, S. P., Atlas, E. L., Toohey, D. W., Alvarado, E. C., Crounse, J. D., Wennberg, P. O., Fisher, M. E., Wold, C. E., Campos, T. L., Adachi, K., Buseck, P. R., and Hao, W. M.: Emissions from forest fires near Mexico City, Atmos. Chem. Phys., 7, 5569–5584, https://doi.org/10.5194/acp-7-5569-2007, 2007.

Yokelson, R. J., Christian, T. J., Karl, T. G., and Guenther, A.: The tropical forest and fire emissions experiment: laboratory fire measurements and synthesis of campaign data, Atmos. Chem. Phys., 8, 3509–3527, https://doi.org/10.5194/acp-8-3509-2008, 2008.

Yokelson, R. J., Crounse, J. D., DeCarlo, P. F., Karl, T., Urbanski, S., Atlas, E., Campos, T., Shinozuka, Y., Kapustin, V., Clarke, A. D., Weinheimer, A., Knapp, D. J., Montzka, D. D., Holloway, J., Weibring, P., Flocke, F., Zheng, W., Toohey, D., Wennberg, P. O., Wiedinmyer, C., Mauldin, L., Fried, A., Richter, D., Walega, J., Jimenez, J. L., Adachi, K., Buseck, P. R., Hall, S. R., and Shetter, R.: Emissions from biomass burning in the Yucatan, Atmos. Chem. Phys., 9, 5785–5812, https://doi.org/10.5194/acp-9-5785-2009, 2009.

Zander, R., Rinsland, C. P., Ehhalt, D. H., Rudolph, J., and Demoulin, P.: Vertical Column Abundances and Seasonal Cycle of Acetylene, C_2H_2, above the Jungfraujoch Station, Derived from IR Solar Observations, J. Atmos. Chem., 13, 359–377, 1991.

Zängl, G. and Hoinka, K. P.: The Tropopause in the Polar Regions, B. Am. Meteorol. Soc., 14, 3117–3139, 2001.

Zeng, G., Wood, S. W., Morgenstern, O., Jones, N. B., Robinson, J., and Smale, D.: Trends and variations in CO, C_2H_6, and HCN in the Southern Hemisphere point to the declining anthropogenic emissions of CO and C_2H_6, Atmos. Chem. Phys., 12, 7543–7555, https://doi.org/10.5194/acp-12-7543-2012, 2012.